1-18-2023

Interfaces in Dynamic Brittle Fracture of PMMA: a peridynamic analysis

Longzhen Wang

Javad Mehrmashhadi

Florin Bobaru

Interfaces in Dynamic Brittle Fracture of PMMA: a peridynamic analysis

Longzhen Wang
University of Nebraska-Lincoln
Javad Mehrmashhadi
University of Nebraska-Lincoln
Florin Bobaru (fbobaru2@unl.edu)
University of Nebraska-Lincoln

Research Article

Keywords: Dynamic fracture, PMMA, peridynamics, interface failure, crack initiation, crack branching

Posted Date: January 18th, 2023

DOI: https://doi.org/10.21203/rs.3.rs-2479564/v1

Additional Declarations: No competing interests reported.

Published (2023) International Journal of Fracture, .
DOI: 10.1007/s10704-023-00731-w

Interfaces in Dynamic Brittle Fracture of PMMA: a peridynamic analysis

Longzhen Wang [a], Javad Mehrmashhadi [a], Florin Bobaru [a, *]

[a] University of Nebraska-Lincoln, Lincoln, NE 68588, United States

* Email of Corresponding Author: fbobaru2@unl.edu

Abstract

Recent experiments in bonded PMMA layers have shown dramatic changes in dynamic crack growth characteristics depending on the interface location and toughness. In this paper we present a peridynamic (PD) analysis of this phenomenon and determine three elements that are essential in a model reproducing the observed fracture behavior: (1) softening near the crack tip to account for changes in PMMA due to heat-generation induced by the high strain rates reached around the crack tip in dynamic fracture; (2) independent extension (mode I) and shear (mode II) modes of fracture; (3) a two-parameter fracture model, which matches both strength and fracture toughness for any horizon size. Once these elements are in place, the PD model captures the experimentally observed dynamic fracture characteristics in bi-layer PMMA: crack branching or not at the interface, depending on the interface location; crack running along the interface for a while before punching through the second PMMA layer; slight crack path oscillations near the far end of the sample. The computed crack speed profiles are close to those measured experimentally. The model produces an enlargement of the fracture process zone when the crack running along the interface penetrates into the second PMMA layer, as observed in the experiments. This is where nonlocality of the PD model becomes relevant and critical.

Keywords: Dynamic fracture, PMMA, peridynamics, interface failure, crack initiation, crack branching

1. Introduction

PMMA (polymethyl methacrylate), also known as acrylic glass, is widely used as an alternative to glass in many industries. To increase PMMA's mechanical performance, several layers are usually bonded together by adhesive. The presence of interfaces affects the fracture behavior. At an interface, a crack may arrest, propagate along it for a while before continuing to grow through the next layer, or not change

its direction, depending on the interface's position, orientation, fracture toughness, and the material properties of the bonded layers [1]. In the recent papers [2], [3], dynamic fracture in bi-layered PMMA, consisting of two PMMA sheets bonded using an acrylic adhesive, has been experimentally studied using Digital Gradient Sensing. It was observed that the failure behavior is strongly influenced, in non-trivial ways, by the interface fracture toughness and its location in the bi-layer system, relative to the pre-crack tip. Trying to computationally explain and predict this behavior is the goal of the present paper.

In classical continuum mechanics, the governing equations are written in terms of partial differential equations (PDEs). When simulating fracture, these models have significant shortages since spatial derivatives are not defined across discontinuities like cracks. To overcome this difficulty, various approaches have been proposed to adjust/redefine the domain as cracks grow. Under the framework of finite element method (FEM), a widely used numerical method to approximate PDE solutions, the element deletion method and cohesive elements have been used to simulate dynamic brittle fracture. In the element-deletion method, all elements that meet certain fracture criterion are deleted. This approach leads to mass loss and has convergence difficulties as the mesh size goes to zero [4]. Cohesive elements need to be predefined along the crack path, which is not known in advance, especially in dynamic fracture problems ([5], [6]). Nonlocal models have been recently shown to correctly predict dynamic brittle fracture behavior in homogeneous materials, including crack branching (see e.g. [7]–[10]). In the present work we offer another example that shows the relevance of using a nonlocal damage model to simulate dynamic fracture.

Peridynamics was introduced as a nonlocal form of continuum mechanics by Silling in 2000 [11] for modeling damage and fracture. Since then, it has been extended to a variety of other problems in which domain changes/discontinuities are part of the problem [12]–[18]. In peridynamics, each material point is connected through peridynamic bonds to other points within a certain neighborhood region called "the horizon". For elasticity, the properties of these bonds are obtained by matching the classical strain energy density under a homogeneous deformation [19].

In the recent work [20], using a bond-based PD model with the simplest brittle bond-failure model but accounting for the heat-affected zone near the crack tip in dynamic fracture of PMMA, we were able to match the observed crack patterns and crack propagation speed in dynamic fracture of monolithic PMMA. In this paper, we show that that model is insufficient to also capture the observed influence a material interface has on the dynamic fracture behavior of bonded PMMA samples. To be able to predict the behavior in the problem with the interface, we need to introduce two additional critical/necessary

components in the model: one that relates to capturing the correct shear deformations and independent modes of fracture, and the other related to capturing not only crack propagation correctly but also crack initiation. The experiments (from [2], [3]) used here to validate our model employ a pre-crack at the tip of the V-notch in the first plate of the PMMA bi-layer, loaded dynamically, but cracks have to initiate in the second, pristine PMMA layer, as well as the interface. As we shall see, a crack initiates along the interface before the crack tip in the first layer reaches the interface.

The paper is organized as follows: Section 2 presents a brief review of peridynamics; in section 3, the experimental tests on bonded PMMA layers from [2] and [3] are briefly reviewed; section 4 discusses the proposed peridynamic model for simulating fracture in PMMA structures with interfaces; in section 5 the numerical results from the proposed PD model are shown and compared with those from the experiments, and the relevance of the nonlocal PD damage model is discussed; in section 6 conclusions are drawn.

In the paper, the following notation for the tensor product and dot product of two vectors $\boldsymbol{p}$ and $\boldsymbol{q}$ will be used, respectively: $(\boldsymbol{p} \otimes \boldsymbol{q})_{ij} = p_i q_j$, and $(\boldsymbol{p} \cdot \boldsymbol{q}) = p_i q_i$.

2. A brief review of peridynamics for deformation and damage

In peridynamics, spatial derivatives are replaced by an integral over a "horizon" region. Mathematical difficulties present in classical models when discontinuities, like cracks, develop in the domain are thus avoided. The PD equations for dynamic problems are:

$$\rho \ddot{\boldsymbol{u}}(\boldsymbol{x}, t) = \int_H \boldsymbol{f}(\boldsymbol{u}(\hat{\boldsymbol{x}}, t) - \boldsymbol{u}(\boldsymbol{x}, t), \hat{\boldsymbol{x}} - \boldsymbol{x})\, dA_{\hat{\boldsymbol{x}}} + \boldsymbol{b}(\boldsymbol{x}, t) \tag{1}$$

where $\ddot{\boldsymbol{u}}(\boldsymbol{x}, t)$ is the acceleration vector field at point $\boldsymbol{x}$ and time t, $\boldsymbol{u}$ is the displacement vector field, $\boldsymbol{b}$ is the body force density, and ρ is the mass density. The integrand $\boldsymbol{f}$ is the peridynamic pairwise force density function that describes the interaction between material points within the nonlocal region, the horizon region H (see Figure 1), defined as:

$$H = \{\hat{\boldsymbol{x}} \in \mathbb{R}^2 : \|\hat{\boldsymbol{x}} - \boldsymbol{x}\| \leq \delta\} \tag{2}$$

where δ is the radius of the normally circular(2D)/spherical(3D) horizon region. The force density between point $\boldsymbol{x}$ and points outside the horizon region is zero.

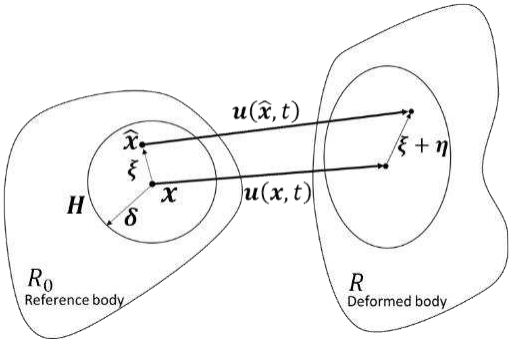

Figure 1 Deformation of a peridynamic bond.

Let $\boldsymbol{\eta} = \boldsymbol{u}(\hat{\boldsymbol{x}}, t) - \boldsymbol{u}(\boldsymbol{x}, t)$ be the relative displacement and $\boldsymbol{\xi} = \hat{\boldsymbol{x}} - \boldsymbol{x}$ the relative position in the reference configuration between two material points of $\hat{\boldsymbol{x}}$ and $\boldsymbol{x}$. From Eq. (2) we have $||\boldsymbol{\xi}|| > \delta \Rightarrow \boldsymbol{f}(\boldsymbol{\eta}, \boldsymbol{\xi}) = \boldsymbol{0}$. When the pairwise force derives from a potential w, a micro-elastic material is defined by the following interaction force:

$$\boldsymbol{f}(\boldsymbol{\eta}, \boldsymbol{\xi}) = \frac{\partial w(\boldsymbol{\eta}, \boldsymbol{\xi})}{\partial \boldsymbol{\eta}} \tag{3}$$

A linear micro-elastic material is obtained if we consider:

$$w(\boldsymbol{\eta}, \boldsymbol{\xi}) = \frac{cs^2||\boldsymbol{\xi}||}{2} \tag{4}$$

where c is called the bond micromodulus and s is the relative elongation of the bond:

$$s = \frac{\|\boldsymbol{\eta} + \boldsymbol{\xi}\| - \|\boldsymbol{\xi}\|}{\|\boldsymbol{\xi}\|} \tag{5}$$

The pairwise force derived from Eq. (3) and Eq. (4) is:

$$\boldsymbol{f}(\boldsymbol{\eta}, \boldsymbol{\xi}) = \begin{cases} cs\dfrac{\boldsymbol{\eta} + \boldsymbol{\xi}}{\|\boldsymbol{\eta} + \boldsymbol{\xi}\|}, & |\boldsymbol{\xi}| \le \delta \\ 0, & |\boldsymbol{\xi}| > \delta \end{cases} \tag{6}$$

The above model is the bond-based PD model, which assumes pairwise interactions do not directly depend on other deformations nearby. As a result, the Poisson's ratio for such a model is pre-determined as 1/3 under 2D plane stress conditions and 1/4 in 2D plane strain and 3D problems [21]. For problems in which the Poisson's ratio value is critical in determining the behavior, the state-based PD model [22][23] or other modified versions of bond-based PD model [24]–[28] can be used. Another limitation of bond-

based PD for modeling failure is that the fracture modes are coupled to each other. In a problem in which this coupling does not match the experimental values for the different fracture modes, one also needs to consider using a more general model, like the state-based PD. In the next section we review one such model, the so-called "enhanced" bond-based PD, which is, as we shall see, a particular case of the state-based PD model.

2.1. The "enhanced" bond-based peridynamics

A particular case of a state-based model is a modified bond-based approach that adds bond rotation as a degree of freedom in the model. This has been called an "enhanced" bond-based peridynamic model [27][28]. With this additional degree of freedom in the tangential direction of the bond, bond rotation is restricted. While not mentioned in [27][28], this model can be considered to be, in fact, as we shall see below, a simplified state-based PD model because only the displacements of the nearest neighbors are used in computing strains at a point, whereas in a state-based model the interaction between two points is determined by the motion of all nodes inside the horizon (see, e.g., [23] page 1174).

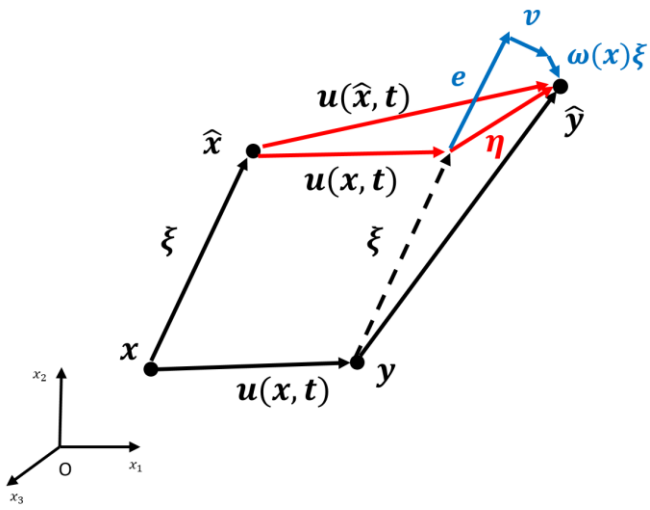

Figure 2 Kinematics in the "enhanced" bond-based PD model (redraw from [29]*).*

As shown in Figure 2, the relative displacement vector $\boldsymbol{\eta}$ can be decomposed into three parts: $\boldsymbol{e}$ corresponds to the bond stretch, $\boldsymbol{v}$ is the bond shear deformation relative to $\boldsymbol{x}$, and $\boldsymbol{\omega}(\boldsymbol{x})\boldsymbol{\xi}$ is the infinitesimal rotation, where $\boldsymbol{\omega}(\boldsymbol{x})$ is the rotation tensor under infinitesimal deformations assumption. The expressions of these quantities are:

$$\begin{aligned} \boldsymbol{e} &= \Big(\big(\boldsymbol{u}(\hat{\boldsymbol{x}},t)-\boldsymbol{u}(\boldsymbol{x},t)\big)\cdot\boldsymbol{n}\Big)\boldsymbol{n} = (\boldsymbol{n}\otimes\boldsymbol{n})(\boldsymbol{u}(\hat{\boldsymbol{x}},t)-\boldsymbol{u}(\boldsymbol{x},t)) \\ \boldsymbol{v} &= \boldsymbol{u}(\hat{\boldsymbol{x}},t)-\boldsymbol{u}(\boldsymbol{x},t)-\boldsymbol{e}-\boldsymbol{\omega}(\boldsymbol{x})\boldsymbol{\xi} \end{aligned} \tag{7}$$

where $\boldsymbol{n} = \frac{\xi}{\|\xi\|}$ is the unit vector along the bond direction.

The bond rotation-angle vector $\boldsymbol{r}$ is defined as:

$$\boldsymbol{r} = \frac{v}{\|\xi\|} = \frac{(\boldsymbol{I}-\boldsymbol{n}\otimes\boldsymbol{n})(\boldsymbol{u}(\hat{\boldsymbol{x}},t)-\boldsymbol{u}(\boldsymbol{x},t))}{\|\xi\|} - \boldsymbol{\omega}(\boldsymbol{x})\boldsymbol{n} \tag{8}$$

For infinitesimal deformations, using the Taylor series expansion of the displacement vector about material point $\boldsymbol{x}$, we have:

$$\begin{aligned} \boldsymbol{u}(\hat{\boldsymbol{x}},t) &\approx \boldsymbol{u}(\boldsymbol{x},\boldsymbol{t}) + (\nabla\boldsymbol{u})(\hat{\boldsymbol{x}}-\boldsymbol{x}) \\ \boldsymbol{\eta} &= (\nabla\boldsymbol{u})\boldsymbol{\xi} = \boldsymbol{\varepsilon}(\boldsymbol{x})\boldsymbol{\xi} + \boldsymbol{\omega}(\boldsymbol{x})\boldsymbol{\xi} \end{aligned} \tag{9}$$

where $\boldsymbol{\varepsilon}(\boldsymbol{x})$ and $\boldsymbol{\omega}(\boldsymbol{x})$ denote the infinitesimal strain tensor and infinitesimal rotation tensor, respectively.

Since $\boldsymbol{\omega}(\boldsymbol{x})$ is skew-symmetric, we have $(\boldsymbol{n}\otimes\boldsymbol{n})\boldsymbol{\omega}(\boldsymbol{x})\boldsymbol{n} = 0$. Using Eq. (9), the bond rotation-angle vector $\boldsymbol{r}$ can be rewritten as:

$$\boldsymbol{r} = \frac{v}{\|\xi\|} = \frac{(\boldsymbol{I}-\boldsymbol{n}\otimes\boldsymbol{n})(\boldsymbol{\varepsilon}(\boldsymbol{x})\boldsymbol{\xi}+\boldsymbol{\omega}(\boldsymbol{x})\boldsymbol{\xi})}{\|\xi\|} - \boldsymbol{\omega}(\boldsymbol{x})\boldsymbol{n} = \frac{(\boldsymbol{I}-\boldsymbol{n}\otimes\boldsymbol{n})}{\|\xi\|}\boldsymbol{\varepsilon}(\boldsymbol{x})\boldsymbol{\xi} \tag{10}$$

where $\boldsymbol{I}$ is the second-order identity tensor.

In this formulation, the elastic micro potential is given by:

$$w(\boldsymbol{\eta},\boldsymbol{\xi}) = \frac{1}{2}cs^2\|\boldsymbol{\xi}\| + \frac{1}{2}\kappa(\boldsymbol{r}\cdot\boldsymbol{r})\|\boldsymbol{\xi}\| \tag{11}$$

where c is the bond elongation micromodulus and κ is the bond shear micromodulus that will be calibrated to the elastic parameters. Because of the geometry of the impact problems studied here (see [3], or Figure 7 below), we use plane stress conditions, with constant micromodulus given by (see [27]):

$$\begin{aligned} c &= \frac{6E}{\pi\delta^3(1-\nu)} \\ \kappa &= \frac{6E(1-3\nu)}{\pi\delta^3(1-\nu^2)} \end{aligned} \tag{12}$$

where E is the elastic Young's modulus, and ν is the given Poisson's ratio.

Using Eq. (9), the bond relative elongation s can be written in terms of the strain tensor $\boldsymbol{\varepsilon}(\boldsymbol{x})$ and rotation tensor $\boldsymbol{\omega}(\boldsymbol{x})$**:**

$$s = \frac{1}{\|\boldsymbol{\xi}\|}\boldsymbol{\eta}\cdot\boldsymbol{n} = (\boldsymbol{\varepsilon}(\boldsymbol{x})\boldsymbol{n})\cdot\boldsymbol{n} + (\boldsymbol{\omega}(\boldsymbol{x})\boldsymbol{n})\cdot\boldsymbol{n} = (\boldsymbol{\varepsilon}(\boldsymbol{x})\boldsymbol{n})\cdot\boldsymbol{n} \tag{13}$$

Here we used the fact that the rotation tensor $\boldsymbol{\omega}$ is skew-symmetric, therefore $(\boldsymbol{\omega}(\boldsymbol{x})\boldsymbol{n}) \cdot \boldsymbol{n}$ is zero. Thus, the bond relative elongation, computed from Eq. (5), is independent of the rotation tensor $\boldsymbol{\omega}$. The calculation of the local strain $\boldsymbol{\varepsilon}$ tensor, which is used to compute the bond rotation-angle vector $\boldsymbol{r}$, is shown in Section 2.3**.**

Using Eq. (3) and Eq. (11), the force density function now becomes:

$$\boldsymbol{f}(\boldsymbol{\eta},\boldsymbol{\xi}) = \frac{\partial w(\boldsymbol{\eta},\boldsymbol{\xi})}{\partial \boldsymbol{\eta}} = \begin{cases} cs\boldsymbol{n} + \kappa(\boldsymbol{I} - \boldsymbol{n}\otimes\boldsymbol{n})\boldsymbol{r}, & |\boldsymbol{\xi}| \le \delta \\ 0, & |\boldsymbol{\xi}| > \delta \end{cases} \tag{14}$$

Notice that $\boldsymbol{f}(\boldsymbol{\eta},\boldsymbol{\xi})$ has two parts, one acting along the bond (elongation) and the other acting perpendicular to the bond direction (related to shear deformation). In order to find the nodal force from Eq. (14), we need $\boldsymbol{r}$ (see Eq. (10)), which requires computing the local strain $\boldsymbol{\varepsilon}$. We explain how the procedure for this calculation works in Section 2.3 at the discrete level. The discretization is discussed in Section 2.2.

Important remark: please note that, while not specified in reference [28], this formulation is valid only for infinitesimal deformations and infinitesimal rotations. These conditions are met in the impact problem discussed in our paper, but for a problem with large deformations, the more general state-based PD model should be used.

2.2. Numerical discretization

The PD equations of motion (see Eq. (1)) can be discretized with a variety of methods [30][31]. Here, we use the meshfree discretization with one-point Gaussian quadrature over the domain [19] which uses a uniform grid with spacing Δx, modified by a scheme to correct for the partial nodal volumes of a uniform grid covered by the circular horizon. Nodes are placed in the center of the cells generated by the uniform grid. We use the partial-volume integration algorithm for the numerical quadrature [32]. A comparison of different partial-volume schemes with an exact computation is given in [33].

Some techniques were introduced in [30] to modify the micromodulus near a boundary to account for the incomplete horizon and reduce the so-called “peridynamic surface effect”. Given the dynamic loading in the tests below, the ‘surface effect’ is expected to have a relatively minor influence on the results (see [34]) and we do not consider such modifications in this study.

We adopt the meshfree discretization to numerically approximate solutions of the PD equations. This numerical method provides great advantages for problems that involve fracture and damage, such as crack branching, fragmentation, etc. [7]. With this method, the spatially discretized version of Eq. (1) is:

$$\rho\ddot{\boldsymbol{u}}_i(t) = \sum_{\boldsymbol{x}_j \in H_i} \boldsymbol{f}(\boldsymbol{x}_j, \boldsymbol{x}_i, t) V_{ij} + \boldsymbol{b}_i \tag{15}$$

where i and j are node numbers, V_{ij} is the volume of node j covered by the horizon of node i.

For the time integration, we use the velocity-Verlet explicit algorithm [35]:

$$\begin{aligned} \dot{\boldsymbol{u}}(t_{n+\frac{1}{2}}) &= \dot{\boldsymbol{u}}(t_n) + \frac{\Delta t}{2}\ddot{\boldsymbol{u}}(t_n) \\ \boldsymbol{u}(t_{n+1}) &= \boldsymbol{u}(t_n) + \Delta t\dot{\boldsymbol{u}}(t_{n+\frac{1}{2}}) \\ \dot{\boldsymbol{u}}(t_{n+1}) &= \dot{\boldsymbol{u}}(t_{n+\frac{1}{2}}) + \frac{\Delta t}{2}\ddot{\boldsymbol{u}}(t_{n+1}) \end{aligned} \tag{16}$$

where subscript n is the time step number, and $\boldsymbol{u}$, $\dot{\boldsymbol{u}}$ and, $\ddot{\boldsymbol{u}}$ denote displacement, velocity, and acceleration vectors, respectively.

2.3. Local strain estimation in the discretized "enhanced" bond-based peridynamics

In order to find the nodal force (see Eq. (14)), we need $\boldsymbol{r}$ (see Eq. (10)), therefore we need to compute the local strain $\boldsymbol{\varepsilon}$. Based on the Taylor series expansion in Eq. (9), to obtain the local strain, we need the displacement gradient. To approximate the displacement gradient, one method is to use the finite difference method for nodal displacements of nearest neighbor nodes. Another way is to use a linear curve fit of displacement values of nearest neighbors, and approximate the gradient with a constant tensor of that locally (at the current node) linear displacement field. The latter is adopted in [28] and we follow that here. We explain the procedure in more detail than provided in [28] and also use a more consistent notation than in [28], to improve clarity.

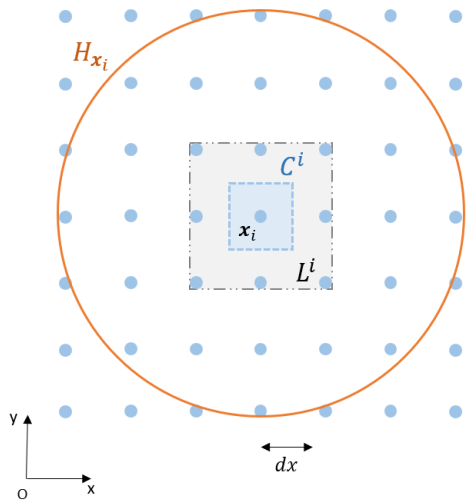

Figure 3 Schematic of cell C^i and local region L^i.

We specify the cell $C^i = \{\hat{\boldsymbol{x}} \in \mathbb{R}^2 : \|\hat{\boldsymbol{x}} - \boldsymbol{x}_i\|_\infty \leq \frac{1}{2}dx\}$, which has a square shape and contains the node i as the center. We also define the "local region" of node $\boldsymbol{x}_i$, $L^i = \{\hat{\boldsymbol{x}} \in \mathbb{R}^2 : \|\hat{\boldsymbol{x}} - \boldsymbol{x}_i\|_\infty \leq dx\}$, which contains node i and its nearest neighbors [28]. For a uniform grid, L^i contains up to 9 nodes in 2D and 27 nodes in 3D. The schematic of C^i and L^i are shown in Figure 3. The linear displacement approximation at some $\boldsymbol{x}$ in cell C^i is, therefore, assumed to be:

$$\bar{\boldsymbol{u}}^i(\boldsymbol{x}, t_{n+1}) = \boldsymbol{m}^i(t_{n+1})\boldsymbol{x}(t_{n+1}) + \boldsymbol{c}^i(t_{n+1}) \tag{17}$$

where $\bar{\boldsymbol{u}}^i(\boldsymbol{x}, t_{n+1})$ is the approximation of the displacement field in the cell C^i at time t_{n+1}, $\boldsymbol{m}^i(t_{n+1})$ is a matrix whose entries are obtained from a linear curve fit of displacements of nodes in L^i at time t_{n+1}, and $\boldsymbol{c}^i$ is the vector corresponding to the rigid body motion. In this section, the estimated strain and the coefficient matrix $\boldsymbol{m}^i$ are at a fixed time step. Therefore, to make the expression more concise, t_{n+1} is not explicitly shown in the following equations.

By taking the derivative of this approximate displacement field $\bar{\boldsymbol{u}}^i$, we find the local constant strain $\boldsymbol{\varepsilon}^i$ at node i. As shown below, $\boldsymbol{\varepsilon}^i$ is expressed in terms of the constant coefficient matrix $\boldsymbol{m}^i$ at a fixed time step t_{n+1}:

$$\varepsilon^i_{\alpha\beta} = \frac{1}{2}\left(\frac{\partial \bar{u}^i_\alpha}{\partial x_\beta} + \frac{\partial \bar{u}^i_\beta}{\partial x_\alpha}\right) = \frac{1}{2}(m^i_{\alpha\beta} + m^i_{\beta\alpha}) \tag{18}$$

where $m^i_{\alpha\beta}$ are the components of the coefficient matrix $\boldsymbol{m}^i$ corresponding to node i, with $\alpha, \beta = 1,2$ for 2D cases, and $\alpha, \beta = 1,2,3$ for 3D cases.

To obtain the components of the matrix $\boldsymbol{m}^i$, we use the displacement of nodes in L^i. In 2D, for example, there are two displacement components, along the x_1 and x_2 directions. As an example, obtaining the coefficients in Eq. (17) in the x_1 direction, can be setup as a linear curve-fitting problem:

$$\bar{u}_1^i = m_{11}^i x_1 + m_{12}^i x_2 + c_1^i \tag{19}$$

where $\bar{u}_1^i$ is the estimated node displacement in x_1 direction, m_{11}^i, m_{12}^i, and c_1^i are the coefficients to be found. The data set used to fit the curve is the position and displacements of the nodes inside L^i. To find the linear best fit to the given set of data points, the linear least squares method is used. The optimal parameters (m_{11}^i, m_{12}^i, and c_1^i) are found by minimizing the sum of squared residuals S^i, as shown below:

$$S^i = \sum_{I=1}^{K^i} (u_1^{i(I)} - \bar{u}_1^{i(I)})^2 \tag{20}$$

where K^i is the total number of nodes inside the local region L^i, superscript (I) is the local node index inside L^i, $u_1^{i(I)}$ is the displacement calculated by Eq. (16) and $\bar{u}_1^{i(I)}$ is the estimated displacements, along the x_1 direction.

To write the linear curve-fitting problem Eq. (20) in matrix forms, we have $\boldsymbol{M}_1^i = [m_{11}^i, m_{12}^i, c_1^i]^T$ denoting the column vector which contains elements in the coefficient matrix $\boldsymbol{m}^i$ and vector $\boldsymbol{c}^i$, and $\boldsymbol{U}_1^i = [u_1^{i(1)}, u_1^{i(2)}, \dots, u_1^{i(K)}]^T$ representing the column vector of nodal displacements along x_1 direction, and $\boldsymbol{X}^i$ containing the nodal coordinates, as shown below:

$$\boldsymbol{X}^i = \begin{bmatrix} x_1^{i(1)} & x_2^{i(1)} & 1 \\ x_1^{i(2)} & x_2^{i(2)} & 1 \\ \vdots & \vdots & \vdots \\ x_1^{i(K)} & x_2^{i(K)} & 1 \end{bmatrix} \tag{21}$$

Eq. (20) can now be written in the following matrix form:

$$S^i = \sum_{I=1}^{K} (u_1^{i(I)} - \bar{u}_1^{i(I)})^2 = \left(\boldsymbol{U}_1^i - \boldsymbol{X}^i \boldsymbol{M}_1^i\right)^T (\boldsymbol{U}_1^i - \boldsymbol{X}^i \boldsymbol{M}_1^i) \tag{22}$$

By taking the derivative of S^i with respect to $\boldsymbol{M}_1^i$, one obtains the 'normal equations' [36] for the minimization problem in Eq. (20):

$$\begin{gathered} \frac{\partial S^i}{\partial \boldsymbol{M}_1^i} = -2\boldsymbol{X}^{iT}\left(\boldsymbol{U}_1^i - \boldsymbol{X}^i \boldsymbol{M}_1^i\right) = 0 \\ \boldsymbol{X}^{iT} \boldsymbol{X}^i \boldsymbol{M}_1^i = \boldsymbol{X}^{iT} \boldsymbol{U}_1^i \end{gathered} \tag{23}$$

$$\boldsymbol{M}_1^i = (\boldsymbol{X}^{i^T}\boldsymbol{X}^i)^{-1}\boldsymbol{X}^{i^T}\boldsymbol{U}_1^i$$

Following a similar process, $\boldsymbol{M}_2^i = [m_{12}^i, m_{22}^i, c_2^i]^T$ which corresponds to the displacement component in x_2 direction is obtained.

$$\boldsymbol{M}_2^i = (\boldsymbol{X}^{i^T}\boldsymbol{X}^i)^{-1}\boldsymbol{X}^{i^T}\boldsymbol{U}_2^i \tag{24}$$

where $\boldsymbol{U_2} = [u_2^{(1)}, u_2^{(2)}, \dots, u_2^{(K)}]^T$ contains nodal displacements along x_2 direction.

Combining $\boldsymbol{M}_1^i$ and $\boldsymbol{M}_2^i$ into the coefficient matrix $\boldsymbol{M}^i = [\boldsymbol{M}_1^i, \boldsymbol{M}_2^i]$, $\boldsymbol{U}_1^i$ and $\boldsymbol{U}_2^i$ into the displacement matrix $\boldsymbol{U}^i = [\boldsymbol{U}_1^i, \boldsymbol{U}_2^i]$, we have:

$$\boldsymbol{U}^i = \begin{bmatrix} u_1^{i(1)} & u_2^{i(1)} \\ u_1^{i(2)} & u_2^{i(2)} \\ \vdots & \vdots \\ u_1^{i(k)} & u_2^{i(k)} \end{bmatrix}, \boldsymbol{M} = \begin{bmatrix} m_{11}^i & m_{21}^i \\ m_{12}^i & m_{22}^i \\ c_1^i & c_2^i \end{bmatrix}$$
$$\boldsymbol{M}^i = (\boldsymbol{X}^{i^T}\boldsymbol{X}^i)^{-1}\boldsymbol{X}^{i^T}\boldsymbol{U}^i \tag{25}$$

In practice, at a certain time step t_{n+1}, the displacement $\boldsymbol{u}(t_{n+1}) = \boldsymbol{u}(t_n) + \Delta t\dot{\boldsymbol{u}}(t_{n+\frac{1}{2}}) = \boldsymbol{u}(t_n) + \Delta t(\dot{\boldsymbol{u}}(t_n) + \frac{\Delta t}{2}\ddot{\boldsymbol{u}}(t_n))$ is calculated based on the displacement, velocity, and acceleration of the previous time step. Then the displacement $\boldsymbol{u}(t_{n+1})$ is used to calculate the coefficient matrix $\boldsymbol{M}^i$ using Eq. (25). After obtaining the coefficient matrix $\boldsymbol{M}^i$, the approximate strains at node i are calculated using Eq. (18). The strain used in Eq. (10) to calculate the rotation angle vector $\boldsymbol{r}$ of bond $\boldsymbol{\xi}_{ij}$ is obtained by averaging the strain of node i and node j. After the bond rotation-angle vector $\boldsymbol{r}$ is calculated with Eq. (10), the pairwise force is updated using Eq. (14). With the new pairwise force, the acceleration $\ddot{\boldsymbol{u}}(t_{n+1})$ and the velocity $\dot{\boldsymbol{u}}(t_{n+1})$ are computed.

Compared with state-based peridynamics, where the force in bond $\boldsymbol{\xi}_{ij}$ depends on the displacements of all points in the horizon of node i and horizon of node j, only the displacements of the nearest neighbor of node i and node j are used to approximate the local strain and calculate the bond force. Therefore, this model can be seen as *a particular case of the state-based model*. In the next section, we discuss damage criteria for bonds.

2.4. Damage criteria for independent modes of fracture

In the regular bond-based peridynamics, damage is modeled using the critical bond relative elongation, allowing a bond to break and no longer sustain a force once the damage criterion is met [19]. Modes of fracture (for example, mode I and mode II) are coupled in bond-based PD, and the coupling may not

always be close to the actual values for modes I and II. Moreover, especially for shear failure under small-displacements, some bonds remain unbroken and bridge a shear crack, when they shouldn't (see [37]), and this happens for the "enhanced" bond-based model unless we introduce a specific mode II failure using the bond shear angle.

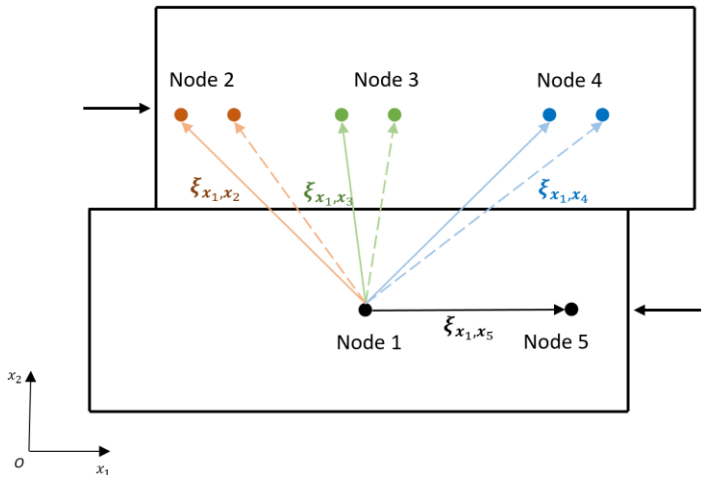

Figure 4 Configuration of bonds before and after a shear deformation (redraw from [38]*).*

As shown in Figure 4, observe three bonds ($\boldsymbol{\xi}_{x_1,x_2}$, $\boldsymbol{\xi}_{x_1,x_3}$, $\boldsymbol{\xi}_{x_1,x_4}$), connecting node 1 with nodes 2, 3, and 4, respectively. Assume a shear deformation moves nodes 2, 3, and 4 to the right. In Figure 4, the dash lines indicate bonds after shear deformation, for which we have $s(\boldsymbol{\xi}_{x_1,x_2}) < 0, s(\boldsymbol{\xi}_{x_1,x_3}) \approx 0, s(\boldsymbol{\xi}_{x_1,x_4}) > 0$. If the critical relative bond elongation is used, exclusively, as a damage criterion, bond $\boldsymbol{\xi}_{x_1,x_4}$ might break, but bonds $\boldsymbol{\xi}_{x_1,x_2}$ and $\boldsymbol{\xi}_{x_1,x_3}$ will not break under this pure mode II deformation. If we were to directly use the angle change between the initial and deformed bonds, we can see from Figure 4 that there is no unique angle change related to the imposed shear deformation. This is why we need to introduce the "bond shear angle", as presented in [38], [29] and explained below.

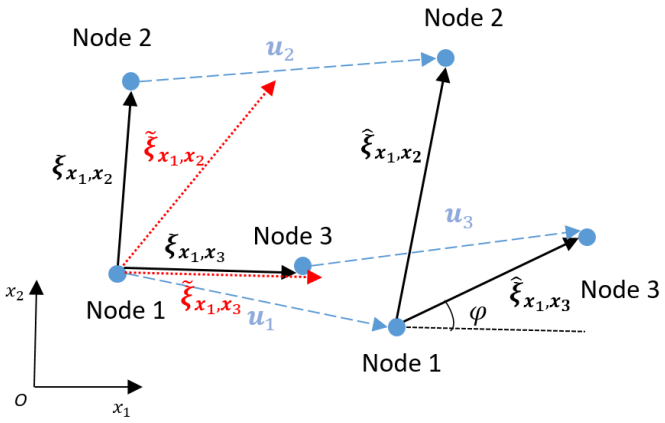

Figure 5 Diagram of bond shear angle computation.

In addition to calculating the bond relative elongation, another bond direction is needed to form an angle that can capture angle changes due to shear deformations. For example, to evaluate $\boldsymbol{\xi}_{\boldsymbol{x}_1,\boldsymbol{x}_2}$ in Figure 5, we select another bond $\boldsymbol{\xi}_{\boldsymbol{x}_1,\boldsymbol{x}_3}$ called 'reference bond'. Both bonds share the same starting point (node 1). After deformation, the two bonds stretch, rotate, and become $\hat{\boldsymbol{\xi}}_{\boldsymbol{x}_1,\boldsymbol{x}_2}$and $\hat{\boldsymbol{\xi}}_{\boldsymbol{x}_1,\boldsymbol{x}_3}$. To calculate the angle change, we first rotate $\hat{\boldsymbol{\xi}}_{\boldsymbol{x}_1,\boldsymbol{x}_3}$ to make its direction coincide with $\boldsymbol{\xi}_{\boldsymbol{x}_1,\boldsymbol{x}_3}$.

The rotation from $\hat{\boldsymbol{\xi}}_{\boldsymbol{x}_1,\boldsymbol{x}_3}$ to $\boldsymbol{\xi}_{\boldsymbol{x}_1,\boldsymbol{x}_3}$ can be described by a rotation matrix $\boldsymbol{R}$**:**

$$\begin{aligned} \frac{\hat{\boldsymbol{\xi}}_{\boldsymbol{x}_1,\boldsymbol{x}_3}}{\left\|\hat{\boldsymbol{\xi}}_{\boldsymbol{x}_1,\boldsymbol{x}_3}\right\|} &= \boldsymbol{R}\frac{\boldsymbol{\xi}_{\boldsymbol{x}_1,\boldsymbol{x}_3}}{\left\|\boldsymbol{\xi}_{\boldsymbol{x}_1,\boldsymbol{x}_3}\right\|} \\ \boldsymbol{R} &= \begin{bmatrix} \cos\varphi & -\sin\varphi \\ \sin\varphi & \cos\varphi \end{bmatrix} \end{aligned} \tag{26}$$

where φ is the direction change of $\boldsymbol{\xi}_{\boldsymbol{x}_1,\boldsymbol{x}_3}$ under the deformation. Notice that $\boldsymbol{R}$ includes the bond rotation caused by infinitesimal rotation $\boldsymbol{\omega}(\boldsymbol{x})$ and bond shear deformation $\boldsymbol{v}$ shown in Section 2.1.

By multiplying $\boldsymbol{R}^{-1}$ to $\hat{\boldsymbol{\xi}}_{\boldsymbol{x}_1,\boldsymbol{x}_3}$ and $\hat{\boldsymbol{\xi}}_{\boldsymbol{x}_1,\boldsymbol{x}_2}$, we have:

$$\begin{aligned} \tilde{\boldsymbol{\xi}}_{\boldsymbol{x}_1,\boldsymbol{x}_3} &= \boldsymbol{R}^{-1}\hat{\boldsymbol{\xi}}_{\boldsymbol{x}_1,\boldsymbol{x}_3} \\ \tilde{\boldsymbol{\xi}}_{\boldsymbol{x}_1,\boldsymbol{x}_2} &= \boldsymbol{R}^{-1}\hat{\boldsymbol{\xi}}_{\boldsymbol{x}_1,\boldsymbol{x}_2} \\ \boldsymbol{R}^{-1} = \boldsymbol{R}^{T} &= \begin{bmatrix} \cos\varphi & \sin\varphi \\ -\sin\varphi & \cos\varphi \end{bmatrix} \end{aligned} \tag{27}$$

Now we have $\tilde{\boldsymbol{\xi}}_{\boldsymbol{x}_1,\boldsymbol{x}_3}$ along the same direction as $\boldsymbol{\xi}_{\boldsymbol{x}_1,\boldsymbol{x}_3}$. We can use $\tilde{\boldsymbol{\xi}}_{\boldsymbol{x}_1,\boldsymbol{x}_2}$ and $\tilde{\boldsymbol{\xi}}_{\boldsymbol{x}_1,\boldsymbol{x}_3}$ to calculate the change of angle formed by $\boldsymbol{\xi}_{\boldsymbol{x}_1,\boldsymbol{x}_2}$ and $\boldsymbol{\xi}_{\boldsymbol{x}_1,\boldsymbol{x}_3}$ due to deformation.

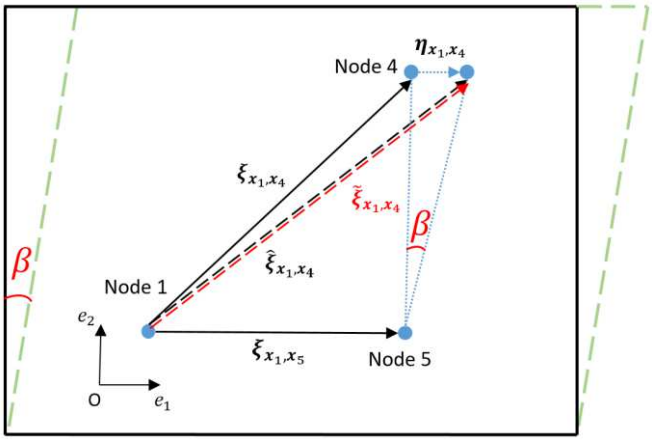

Figure 6 Bond shear angle: 2D simple shear case (redraw from [38]*).*

As shown in Figure 6, we take the bond $\boldsymbol{\xi}_{\boldsymbol{x}_1,\boldsymbol{x}_4}$ in Figure 4 as an example. By applying a uniform shear angle β to the 2D body, the bond $\boldsymbol{\xi}_{\boldsymbol{x}_1,\boldsymbol{x}_4}$ changes in both length and direction under the simple shear deformation. For convenience, the locations of node 1 before and after deformation are assumed to coincide. We choose a horizontal bond $\boldsymbol{\xi}_{\boldsymbol{x}_1,\boldsymbol{x}_5}$, whose direction does not change under simple shear, as the reference bond. Since the direction of $\boldsymbol{\xi}_{\boldsymbol{x}_1,\boldsymbol{x}_5}$ does not change, the rotation matrix $\boldsymbol{R}$ is the identity matrix. Therefore, in this case, $\tilde{\boldsymbol{\xi}}_{\boldsymbol{x}_1,\boldsymbol{x}_4} = \boldsymbol{R}^{-1}\hat{\boldsymbol{\xi}}_{\boldsymbol{x}_1,\boldsymbol{x}_4}$ is the same as $\hat{\boldsymbol{\xi}}_{\boldsymbol{x}_1,\boldsymbol{x}_4}$.

The shear angle β of bond $\boldsymbol{\xi}_{\boldsymbol{x}_1,\boldsymbol{x}_4}$ is, in general, computed by:

$$\beta = \left| \frac{(\tilde{\boldsymbol{\xi}}_{\boldsymbol{x}_1,\boldsymbol{x}_4} - \boldsymbol{\xi}_{\boldsymbol{x}_1,\boldsymbol{x}_4}) \cdot \boldsymbol{e_1}}{\boldsymbol{\xi}_{\boldsymbol{x}_1,\boldsymbol{x}_4} \cdot \boldsymbol{e_2}} \right| \tag{28}$$

where $\boldsymbol{e_1}$ is the unit vector parallel to $\boldsymbol{\xi}_{\boldsymbol{x}_1,\boldsymbol{x}_5}$ and $\boldsymbol{e_2}$ is perpendicular to $\boldsymbol{e_1}$. Since all three bonds in Figure 4 have the same elongation along $\boldsymbol{e_1}$ and same component along $\boldsymbol{e_2}$, the three bonds will have the same bond shear angle β under the shear deformation in Figure 4.

The critical bond relative elongation and critical bond shear angle are separately calibrated to the modes I and II (using the G_{IC} and G_{IIC} experimentally measured values). With the constant micromodulus given in Eq. (12), one obtains the critical relative elongation s_c and critical shear angle θ_c for plane stress conditions as (see [29]):

$$s_c = \sqrt{\frac{2G_{IC}}{c\delta^4}} \tag{29}$$

$$\beta_c = \sqrt{\frac{240 G_{IIC}}{(8c + 7\kappa)\delta^4}}$$

The bond between node i and node j is broken when the relative elongation or the shear angle exceeds their critical values:

$$\mu(\boldsymbol{x}_i - \boldsymbol{x}_j) = \begin{cases} 1, & \mathrm{s} \le s_{\mathrm{c}} \text{ and } \beta \le \beta_{\mathrm{c}} \\ 0, & \mathrm{s} > s_{\mathrm{c}} \text{ or } \beta > \beta_{\mathrm{c}} \end{cases} \tag{30}$$

To plot the evolution of damage in simulations, a useful damage-related quantity is the damage index of a node i , which is a scalar defined as the ratio of the number of broken bonds and the total number of bonds for node i. The value for the damage index varies between zero and one (fully damaged):

$$\varphi(\boldsymbol{x}_i) = 1 - \frac{\sum_{\boldsymbol{x}_j \in H_i} \mu(\boldsymbol{x}_i - \boldsymbol{x}_j)}{\sum_{\boldsymbol{x}_j \in H_i} 1} \tag{31}$$

3. Review of experimental test results

The dynamic fracture of bi-layered PMMA samples was studied using Digital Gradient Sensing (DGS) technique [3]. The bi-layer PMMA samples were made by bonding two PMMA samples using acrylic adhesive (Weld-on 16). Material properties for PMMA and the adhesive used are shown in Table I. By varying the adhesive thicknesses between the PMMA layers (25µm and 100µm), a strong (thin layer) or weak (thick layer) interface is obtained. The impact loading, generated by a striker and a long bar, is transferred into PMMA via two faces of a V-notch. At the end of the V-notch, there is a pre-crack with a 2 mm length (cut by razor blade). During the crack propagation, the crack path is captured by 32 images which is used to estimate the average crack velocity. The dimension of the bi-layered PMMA specimen is illustrated in Figure 7.

At the impact speeds used in [3], crack branching was observed in both cases: strong and weak interface. Interestingly, in the weak interface case (d=28 mm from the initial crack tip), the crack travels along the interface a short while (~12 mm) before continuing its growth into the second layer as two cracks commencing from the tips of the interface crack. For the strong interface (d=28 mm from the initial crack tip), the crack propagation along the interface is significantly shorter (4 mm).

As shown in Figure 8, as the interface location changes (weak interface at d=7 mm, 17 mm, 42 mm from the pre-crack tip), the crack paths and the angle between the two daughter cracks are very different. In each case, the crack propagated under mostly mode-I conditions until it reaches the interface. For all

configurations except d=7 mm, the mode-I crack reaches the interface, then branches into two symmetric daughter cracks (with respect to the horizontal direction), propagating upward and downward along the interface. In the cases d=17 mm and 42 mm, the interface crack (which grows under mixed-mode conditions but dominated by mode II) travels around 2 mm and 22 mm, respectively. After growing along the interface for a while, both cracks penetrate the second PMMA layer simultaneously. Also, the two daughter cracks growing in the second layer have initial angles between $\pm 28^{\circ}$ and $\pm 11^{\circ}$ relative to the horizontal direction.

For all cases, mode-mixity $tan^{-1}\frac{K_{II}}{K_I}$ is close to zero before the crack reaches the interface and after it passes through it. However, for all cases except d=7mm, mode-mixity has a steep increase as the crack reaches the interface, meaning that crack growth happens under mixed-mode conditions at the interface. These experimental observations show that the interface properties and interface location have significant influence on the PMMA fracture behavior [3].

Table I Material properties for PMMA and adhesive (from [3]*).*

	PMMA	Weld-on 16 acrylic Adhesive
Young's Modulus, GPa	5	2.85
Poisson's ratio	0.35-0.4	---
Fracture Toughness K_{Ic}, MPa.m$^{0.5}$	1.31	1.01 (Strong Interface)
		0.68 (Weak Interface)
Fracture Toughness K_{IIc}, MPa.m$^{0.5}$	1.44	2.20 (Weak Interface) 3 (Strong Interface, assumed)
Density, kg/m^3	1010	---
Thickness, mm	---	0.025 (Strong Interface)
		0.1 (Weak Interface)
Tensile Strength (MPa)	70 MPa	23 MPa (Weak Interface) 50 MPa(Strong Interface, assumed)

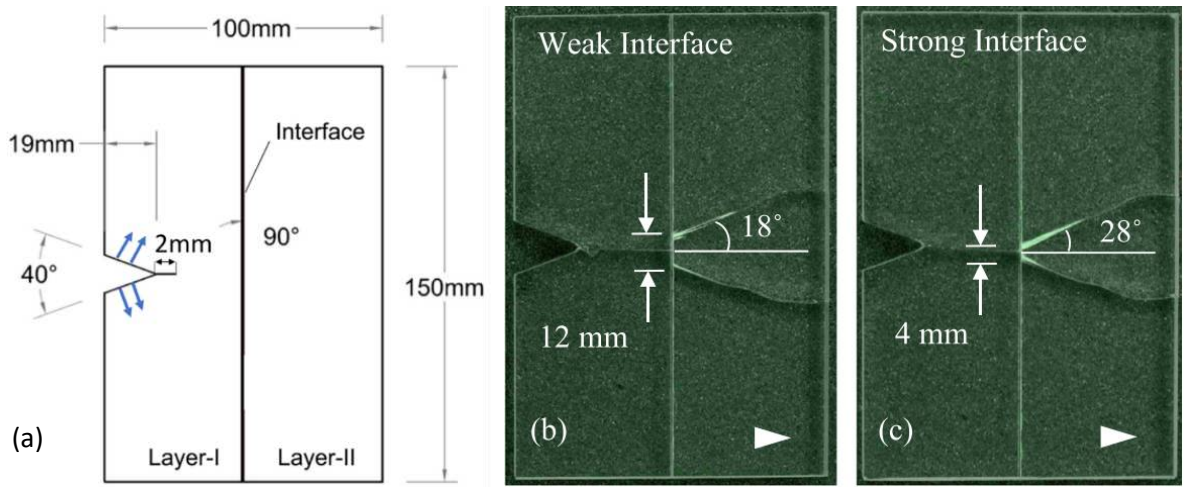

Figure 7 Photographs of fractured specimens showing crack path selection in (a) Configurations and the associated specimen geometry (from [3]*) (b) 'Weak' 90° layered configuration (c) 'Strong' 90° layered configuration. Arrowhead indicates crack growth direction (from* [3]*).*

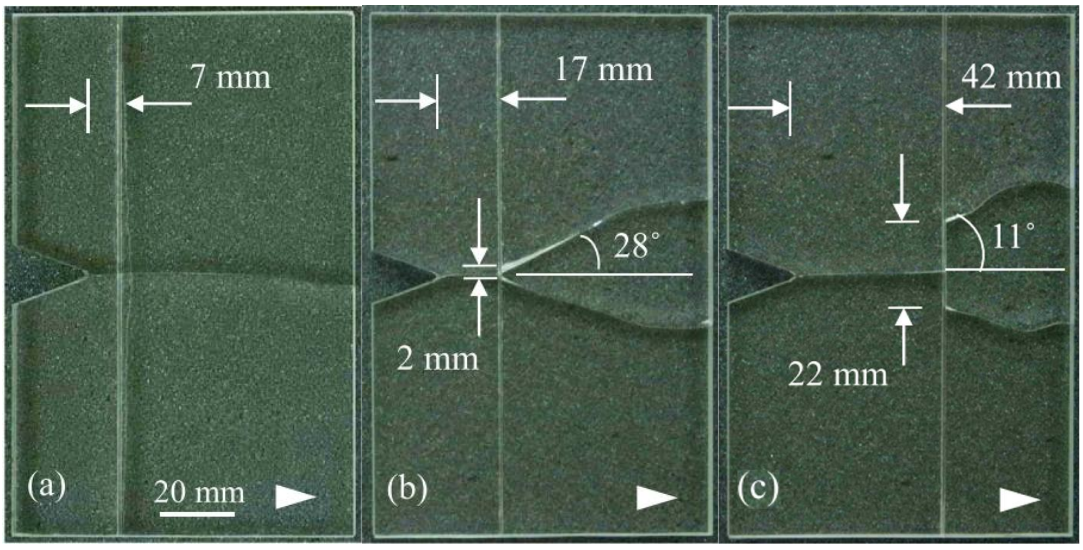

Figure 8 Photographs of fractured specimens showing crack path selection in d=(a) 7 mm, (b) 17 mm, (c) 42 mm (from [2]*).*

4. Peridynamic modeling of PMMA bi-layer under dynamic impact

4.1. Loading conditions

In this paper, we use the same loading condition as our previous study in monolithic PMMA simulation [20]. We simulated the impact experiment with a 3-D LS-DYNA model in [20] to obtain the impact pressure on the surface of the V-notch (see Figure 9) using a dynamic solver. Notice that if the contact is not ideal,

only a certain percentage area of V-notch is in contact with the long bar. In such a case, the impact pressure may not necessarily be evenly distributed on the surface. In this paper, we simplify the loading condition by assuming the impact pressure is evenly distributed along the contact part of the V-notch.

We used the pressure pulse from the LS-DYNA model to identify the fracture initiation time, t_f, and the corresponding pressure. Since the experimental loading was unclear after PMMA crack initiation, several different load conditions were compared in our previous work [20]. We concluded that the loading condition that dropped gradually produced consistent crack propagation speed with the monolithic PMMA experiment and the PMMA split fully. Therefore, we use the gradual decrease in loading as used in our previous work [20] (see Figure 9).

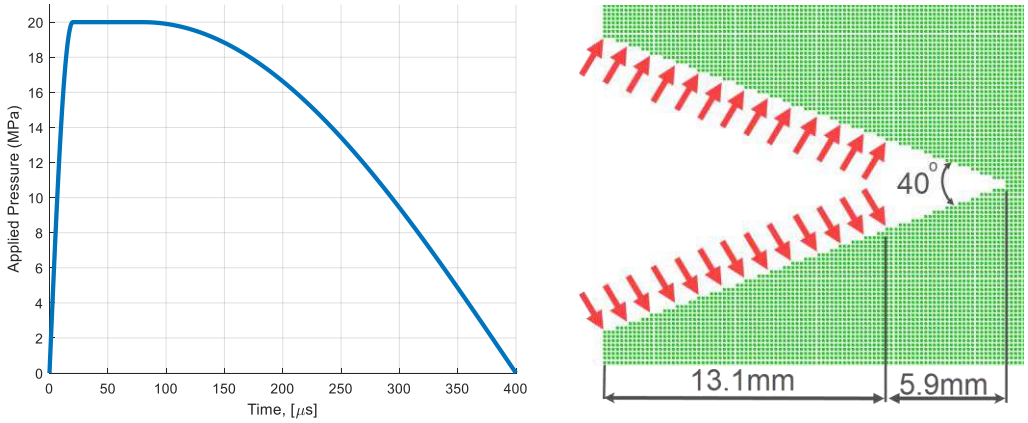

Figure 9 (a) The impact pressure profile ([20]) used in all simulations in this work, (b) PD nodes on the part of the V-notch surface subjected to body forces converted from the pressure profile.

4.2. The PD model accounting for PMMA softening due to heating near the crack tip

In the dynamic fracture experiment on PMMA, the temperature rise at the propagating crack tip has been observed and measured [39]. The heating near the crack tip is the result of polymer crazing. As the craze fibrils form, there is significant molecular chain motion in the active layer [40]. Eventually, the molecular chain scission [40] and pull-out from surrounding material [41] happens during the failure of craze fibrils. All these processes of the polymer craze can generate heat.

The temperature at the tip of a running crack in PMMA can get as high as 530 °C , higher than the glass transition temperature for this material [42]. Based on the result of experimental measurements and molecular dynamics simulations ([43], [44]), Young's modulus of PMMA drops from 5.02 GPa at room temperature to 0.56 GPa at 650 K (see Table II).

Table II Young's modulus of PMMA under different temperature ([43]*,* [44]*).*

T (K)	200	250	300	350	400	450	500	550	600	650
E (GPa)	5.02	4.29	3.81	3.52	3.11	2.71	1.25	1.25	0.79	0.56

In our previous work [20], we proposed and tested a PD model that considered thermal softening around the crack tip. The area in which the temperature increased is called the "Heat Affected Zone" (HAZ). A rule for how large should the HAZ be relative to the nonlocal region size in our PD model is given in [20].

To roughly estimate the extent of the HAZ during dynamic fracture, we analytically solve the heat transfer over the time scale relevant to the dynamic crack propagation problem. Our aim is to find how deep a significant temperature rise penetrates into the material around the tip of the crack, assuming that at the crack tip we have a fixed temperature.

The 1D diffusion problem we solve is the following [45]:

$$\frac{\partial\theta(x,t)}{\partial t} = k\frac{\partial^2\theta(x,t)}{\partial x^2}$$
$$\theta(x,0) = f(x), \qquad \theta(0,t) = T_1, \qquad \theta(L,t) = T_2 \tag{32}$$

where $\theta(x,t)$ is the temperature (℃) at point x and time t, k is the thermal diffusivity $m^2/_S$, $f(x)$ is the initial condition, L is the length (m) of the 1D bar and T_1 and T_2 are boundary conditions at $x = 0$ and $x = L$, respectively.

The solution to Eq. (32) can be obtained with the separation of variables [46]:

$$\theta(x,t) = T_1 + \frac{(T_2 - T_1)}{L}x + \sum_{n=1}^{\infty} D_n \sin\left(\frac{n\pi x}{L}\right) e^{-k\left(\frac{n\pi}{L}\right)^2 t}$$
$$D_n = \frac{2}{L}\int_0^L (f(x) - T_1 - \frac{(T_2 - T_1)}{L}x)\sin\left(\frac{n\pi x}{L}\right)dx \tag{33}$$

We set the diffusion coefficient of PMMA to be $k = 1.35 \times 10^{-7}\,\frac{\mathrm{cm}^2}{\mathrm{s}}$ [47], a sufficiently large $L = 0.1\mathrm{m}$, initial temperature of $f(x) = 25$ ℃ ,and the boundary conditions of $T_2 = 25$ ℃, and $T_1 = 377$ ℃ (= 650 K) corresponding to the softening of 0.5 GPa in Table II). In Figure 10, we show the temperature distribution at 5, 10, 20, and 50 μs. At an approximately 300 m/s crack propagation speed in PMMA (see [2]), the crack advances 1.5 mm in 5 μs. During this time interval, no significant increase in temperature

is noticed for points which are more than 3 µm away from the crack tip. Notice that the result matches well with the observation in [39]: the size of the heat affect zone is in the order of 3 µm. Our results show that thermal diffusion, in our example, is sufficiently slow compared with dynamic fracture. Over the duration of crack propagation, the heated zone relevant to the dynamic crack growth problem is limited to a small region around the crack tip. Therefore, in our study, we assume that the size of heated zone is constant during the dynamic fracture.

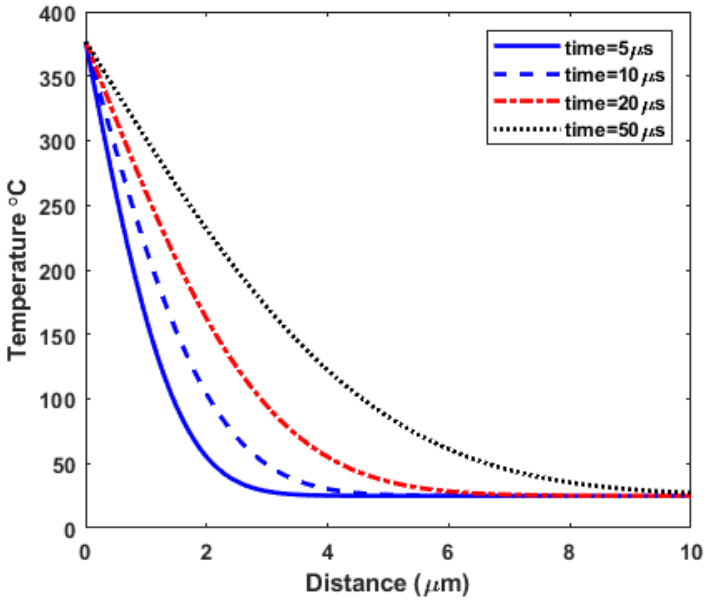

Figure 10 Temperature distribution at 5, 10,20, and 50 µs simulated in a 1D problem using boundary conditions of $T_1 = 377\ °C$, and $T_2 = 25\ °C$.

4.3. Locating the fracture process zone

To apply the HAZ at the crack tip, we need to first determine the crack tip location ($\boldsymbol{x}_{\text{tip}}$) at each solution time-step (n). We use the strain energy density values (w_i) at each node and time step ($n-1$), calculated as follows:

$$w_i = \int_{H_i} w(\boldsymbol{\xi}, \boldsymbol{\eta}; t_{n-1}) \tag{34}$$

We calculate the value of w_i using $w(\boldsymbol{\xi}, \boldsymbol{\eta})$ for unbroken bonds from the previous solution step to locate $\boldsymbol{x}_{\text{tip}}$, defined here as the node with the highest w_i value. After locating $\boldsymbol{x}_{\text{tip}}$, we define the HAZ to be a circle centered at $\boldsymbol{x}_{\text{tip}}$ with a radius r_{HAZ} equal to $2 \times \delta$ [20]. When we compute the pairwise force on each bond, we first test whether the bond is inside HAZ. We define a parameter λ_{HAZ} that decides

whether a bond is inside the HAZ or not, based on the distances $d_{\boldsymbol{x}}$ and $d_{\hat{\boldsymbol{x}}}$ of nodes $\boldsymbol{x}$ and $\hat{\boldsymbol{x}}$ to node $\boldsymbol{x}_{\text{tip}}$ as follows (see Figure 11):

$$\lambda_{HAZ}(\boldsymbol{x}, \hat{\boldsymbol{x}}) = \begin{cases} 1, & d_{\boldsymbol{x}} \le r_{HAZ} \ \text{and} \ d_{\hat{\boldsymbol{x}}} \le r_{HAZ} \\ 0, & \text{otherwise} \end{cases} \tag{35}$$

Since bond rotations are also considered in our model, the constitutive model for PMMA bonds inside the HAZ is different from our previous work (see [20]). Here, the PMMA bonds in the HAZ are assumed to be given by a bi-linear function (for both the stretch part and shear part), as follows:

$$\boldsymbol{f}(\boldsymbol{\eta}, \boldsymbol{\xi}) = \begin{cases} c[0.1s + 0.09s_0]\boldsymbol{n} + 0.1\kappa(\boldsymbol{I} - \boldsymbol{n}\otimes\boldsymbol{n})\boldsymbol{r}, & \text{if } s > 0.1s_0 \text{ and } \lambda_{\text{HAZ}} = 1 \\ cs\boldsymbol{n} + \kappa(\boldsymbol{I} - \boldsymbol{n}\otimes\boldsymbol{n})\boldsymbol{r}, & \text{otherwise} \end{cases} \tag{36}$$

Note that $\boldsymbol{f}(\boldsymbol{\eta}, \boldsymbol{\xi}) = \boldsymbol{0}$ when $|\boldsymbol{\xi}| > \delta$. We first assume the PD micromodulus is unchanged when the bond relative elongation is smaller than $0.1s_0$ (see Figure 11). As the overstress macromolecules cause local heating, the Young's modulus of PMMA decreases. Therefore, in the HAZ, for the bond which relative elongation is larger than $0.1s_0$, we decrease the micromodulus to $0.1c$ and 0.1κ, according to the measured behavior in [48]. In the previous model [20], we only modify the bond micromodulus c.

Since the fracture energy of PMMA is almost unchanged as the temperature changes [49], it is assumed to be constant in our PD model. To maintain the fracture energy G_0 in bilinear model same as the linear model, the following condition needs to be satisfied (areas under linear and bilinear functions need to match):

$$\frac{1}{2}cs_0{}^2 = \frac{1}{2}c(0.1s_0)^2 + c(0.1s_0)(s_{bi-0} - 0.1s_0) + \frac{1}{2}(0.1c)(s_{bi-0} - 0.1s_0)^2 \tag{37}$$

We find the critical strain s_{bi-0} for the bilinear function is $2.40s_0$.

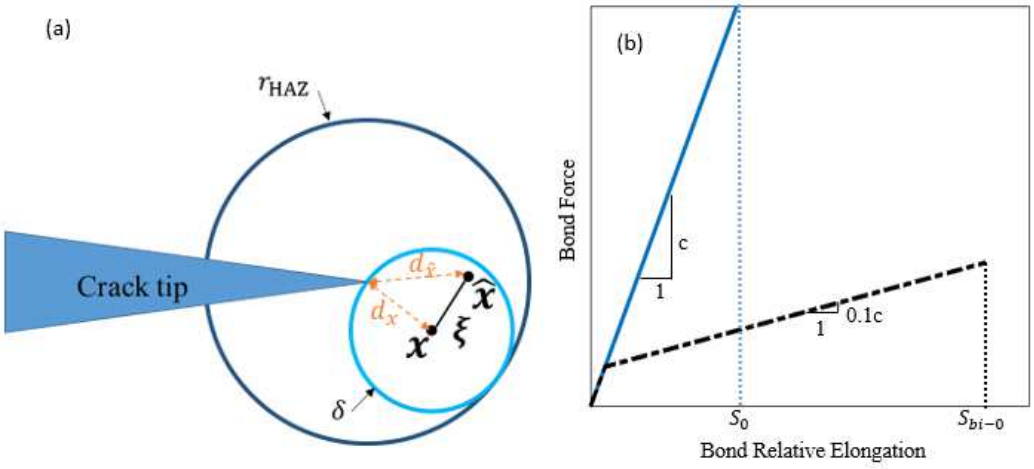

Figure 11 (a) Heat Affect Zone around the crack tip, (b) Linear and bi-linear bond force-relative elongation relation.

4.4. PD interface modeling in bi-layered PMMAs

In the experimental tests [3], bi-layered PMMAs were made by gluing two PMMA together with the acrylic adhesive, Weld-on 16 (see Table I for material properties). Note that the adhesive thickness for the strong interface is 25 μm. If we were to explicitly model the actual adhesive material thickness with the PD model, assuming that thickness to be spanned by a full horizon region (thus around 8 nodes across, if we use a horizon factor of 4, see below), we would end up with more than 400 million nodes and a costly computation. To reduce the computational cost, we instead introduce an approximate way of representing the actual interface, effectively simulating a much thicker interface in the PD model by employing a much larger horizon size and, implicitly, a much coarser discretization grid. In this way we significantly increase the computational efficiency, without, hopefully, qualitatively affecting the results. As we shall see, this hope is realized.

To model the interface, we assign mechanical properties of the interface material to all PD bonds crossing the interface geometrical location, as shown in Figure 12. The micro properties of interface bonds are calibrated to the measured interface properties (Young's modulus and fracture toughness) given in Table I. This approach means that the effective thickness of the interface in the model is twice the horizon size. With the horizon size used in the next section, the effective thickness of the interface in the PD model is 16 and 48 times larger than the actual thickness of the weak and strong interfaces, respectively.

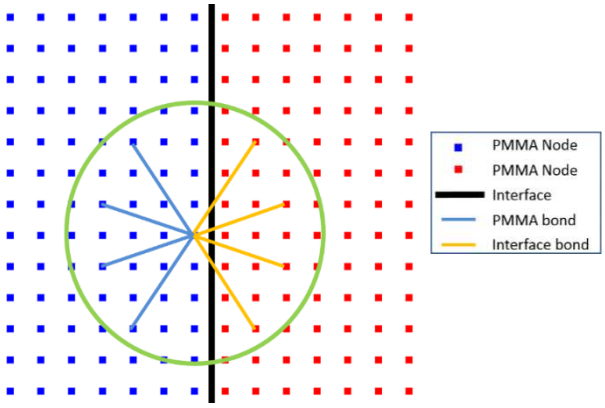

Figure 12 Modeling the adhesive interface: all bonds crossing the interface line are considered to be "interface bonds", calibrated to the material properties of the adhesive used in experiments.

As measured by the uniaxial tensile test in [2], the tensile strength of the weak interface is 23 MPa. Since there is no experimental data for the tensile strength of the strong interface, we assume it to be 50 MPa, larger than that of the weak interface but smaller than PMMA's. For problems in which there is no pre-crack, for example the interface in this study, the strength is independent of the fracture toughness.

To take the interface strength into account, we used the bilinear model proposed in [50]. As shown below, the maximum bond force cs_1 is calibrated to the ultimate strength. Once the bond relative elongation exceeds s_1, the bond is softened and the bond force decreases to 0 at s_c which is calibrated to the energy release rate.

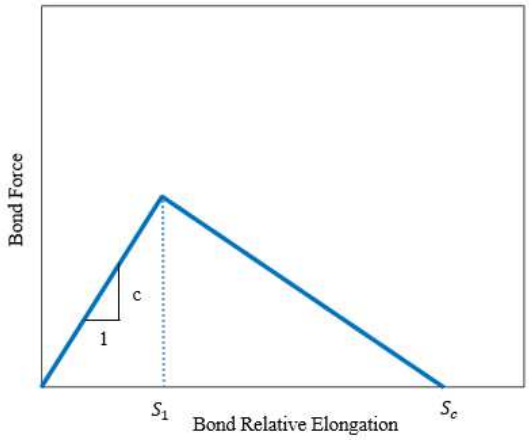

Figure 13 The bilinear model for the tensile part of interface bond force.

Because we have not found any experimental data regarding the dependency of stiffness or fracture toughness of the acrylic adhesive on possible heating at the tip of a dynamically running crack, here we assume no softening of the adhesive around the crack tip. Therefore, we assume that there is no temperature rise and the interface bonds are not influenced by the HAZ. For some results in which we do consider softening of interface bonds as well, please see the Appendix.

Since we only consider the tensile strength of the interface, the shear part of the interface bond force is not affected by the bilinear model. The new constitutive model for interface bonds is shown as follows:

$$\boldsymbol{f}(\boldsymbol{\eta},\boldsymbol{\xi}) = \begin{cases} cs_1 \dfrac{s - s_0}{s_1 - s_0}\boldsymbol{n} + \kappa(\boldsymbol{I} - \boldsymbol{n}\otimes\boldsymbol{n})\boldsymbol{r}, & \text{if } s > s_1 \\ cs\boldsymbol{n} + \kappa(\boldsymbol{I} - \boldsymbol{n}\otimes\boldsymbol{n})\boldsymbol{r}, & \text{if } s < s_1 \end{cases} \tag{38}$$

$$s_1 = \frac{2\sigma_u}{3E}, s_c = \frac{2\pi G_{IC}}{3\sigma_u \delta}$$

where σ_u is the ultimate tensile strength.

5. Numerical Results

In our previous work on dynamic fracture in monolithic PMMA ([20]) we presented δ-convergence (see [51]) results that helped select an appropriate horizon size, based on matching the experimentally

measured crack propagation speed and the morphology of crack paths. In the simulations shown below, we choose that horizon, $\delta = 0.8$ mm. For the discretization, based on previous studies on *m*-convergence ([51]) for dynamic brittle fracture problems (see [52][53]), we choose a value $m = \frac{\delta}{dx} = 4$ for the horizon factor. This value was found to provide a good balance between computational efficiency and independence of the crack path on the grid orientation. We therefore discretize the domain using uniform grid spacing of 0.2 mm, resulting in *m*-factor $\frac{\delta}{dx} = \frac{\delta}{dy} = 4$. The total number of nodes is about 400K. To ensure numerical stability of the computations, the time step for all of the results shown below is set to be 0.02 μs. We use a PD code implemented to run on an Intel Xeon E5-2670 2.60-GHz processor with the Tesla P100 GPU. On this system, the wall-clock time to run most of the examples shown here take about 10-15 minutes to complete. We verified our implementation against Abaqus results for some of the examples shown in [27] and [28] on elastic deformations (uniaxial tension and simple shear for different Poisson ratios – 0.1 and 0.2). These verification results are not shown here for the sake of brevity.

In the following sections we present results with the "full" model, that contains all of the critical components mentioned in the Introduction section. To demonstrate that indeed these components are critical in correctly predicting the dynamic fracture behavior of PMMA with material interfaces, in the Appendix we show simulation results from models that are missing at least one of the three critical components: (1) softening near the crack tip to account for changes in PMMA stiffness due to heat-generation induced by the high strain rates reached around the crack tip in dynamic fracture; (2) independent extension (mode I) and shear (mode II) modes of fracture; (3) a two-parameter fracture model, that can match both strength and fracture toughness for any horizon size (bond failure with a softening phase) to be able to predict initiation as well as crack propagation. Without the softening near crack tip, the simulated crack propagation velocity in PMMA is around twice as fast as the experimentally measured values. The independent modes of fracture and two-parameter fracture model are important to capture the mode II-dominated fracture (along the interface) and crack initiation at the interface and in the second PMMA layer. More details are shown in Appendix.

5.1. Simulation results for the influence of the weak and the strong interface

With the heat affected model and interface model defined in Section 4, the damage maps for the PMMA sample with the two different interface properties are shown in Figure 14. The crack paths of both samples match well with the experiment. In the PMMA sample with the weak interface, the crack travels about 8 mm (3 mm less than the experiment result) along the interface before penetrating the second layer. In

the PMMA sample with the strong interface, the crack travels for 3 mm (1 mm less than the experiment result) along the interface before penetrating the second layer. As the fracture energy of the interface is lower, the interface bond is easier to be broken which leads to a longer crack path along the interface.

For the PMMA sample with the strong interface, the angle between the two branched daughter cracks is ~50^o, which is 12% less than experiment measured angle (~56^o) [3]. For the PMMA sample with the weak interface, the angle between the two branched daughter cracks is ~40^o, which is 11% more than the measured experiment angle (~36^o) [3]. The waviness in crack paths (near the right boundary) is also observed in simulation results and the shape matches well with the experiment results. The difference in the crack angle may be caused by the difference in boundary conditions. In the PD simulations, we assume that the top and bottom edges are free, whereas in the experiment, on the top and bottom edges of the specimen there are putty layers that absorb some of the stress waves and reduce wave reflection back into the specimen. Simulation movies of crack propagation for samples with the interface at 28mm are shown in Movies 1 and 2 (damage index) and 3 and 4 (strain energy density) for the weak and strong interfaces, respectively (see Supplementary Materials).

The comparison between experimental results and simulation results in terms of crack speed is shown in Figure 15. In both cases, the cracks reach the interface around 15 μs later than the experiment result. This is due to the lower crack velocity, compared with experimental measurements, around 150 μs. In both cases, there is a rapid increase in crack velocity when cracks reach the interface and a steep drop as the crack tips get out of the interface.

The drop in crack velocity around 150 μs is not caused by the presence of the interface. Such drop was also observed in monolithic PMMA simulations in our previous research [20]. This drop may be caused by the difference in loading conditions and boundary conditions. The loading condition in the simulation is simplified. The loading conditions in the experiment maybe not be smooth over time, may not be evenly distributed along the notch, and may have different amplitudes. The difference in the boundary conditions (putty strips were used in the experiment on the top and bottom sample edges [2], while we assume stress-free boundaries in the simulations) also affect wave reflections/reinforcement and change the crack velocity.

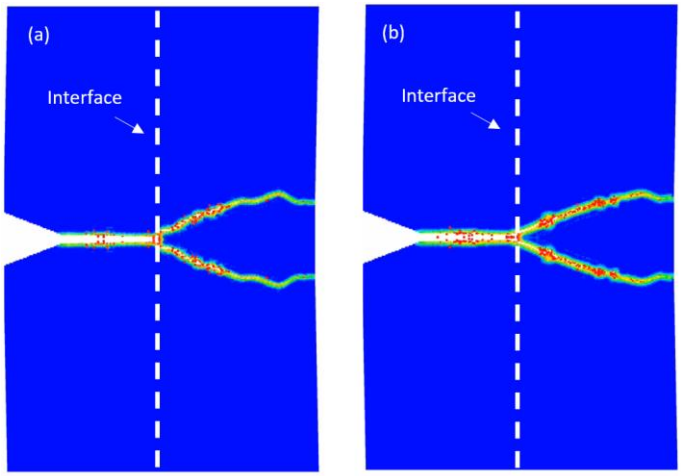

Figure 14 Damage map for bi-layered PMMA with the (a) weak interface and (b) strong interface. PD model finds crack branching in both cases, as seen in experiments. Crack propagate along the weak interface about 8 mm. See also Movies 1 and 2 (damage index), and corresponding strain energy density in Movies 3 and 4.

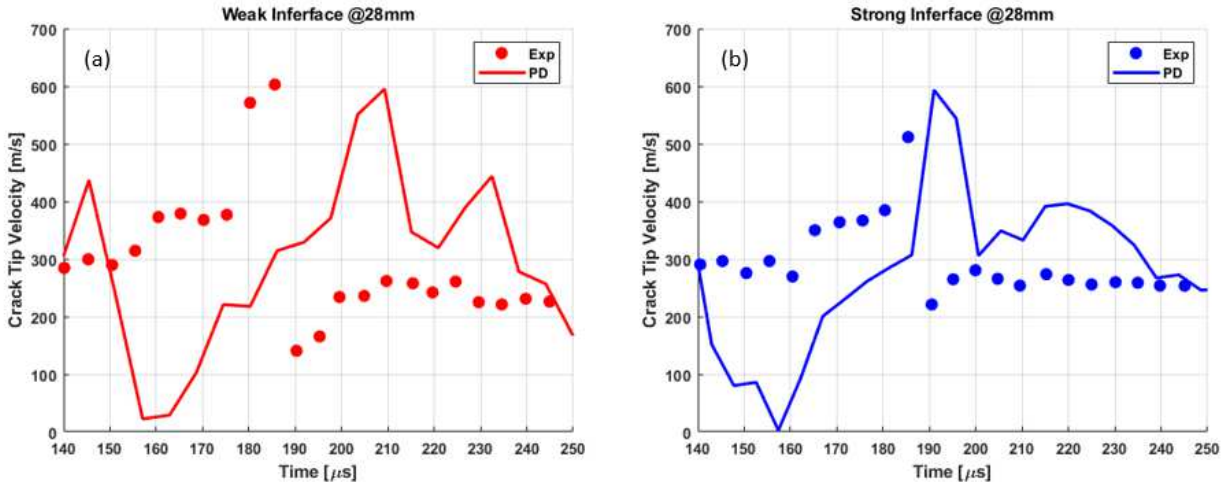

Figure 15 Comparisons of the histories of crack tip propagation speeds for bi-layered PMMA with (a) the weak interface and (b) the strong interface.

5.2. Simulation results on the influence of interface location

In this part, we study the influence the interface location has on the dynamic fracture behavior of the bi-layer PMMA system and discuss the roles different model components play in the simulation results. In Figure 16, we show the damage map of PMMA samples with the weak interface placed at different locations away from the tip of the pre-crack. For the sample with the interface located 7 mm from the pre-crack tip, the crack does not branch at the interface. It penetrates into the second layer and continues

to run straight as a single crack, which is what happened in the experiments as well. In the experimental results reproduced in Figure 8, the crack deviates slightly from its initial straight path near the final third of the specimen (most likely because of slight asymmetries in loading or boundary conditions), but does not branch. For the sample with the interface at 17 mm, the damage map also matches the experimental observations. The angle between the two branched cracks is ~54^o, very close to that measured from the experiments (56^o) [2]. For the sample with the interface at 42 mm, the crack branches at the interface, and travels for about 20 mm along it. In the experiments, the crack runs along the interface for 22 mm. The angle between the two branched cracks is ~23^o, very close to the experimental measurements (22^o) [2]. The damage maps are similar to the experiment results, and they show the same trend: the farther the interface is from the pre-crack tip, the longer the crack travels along the interface. The evolution of crack propagation for these samples is shown in Movies 5-7 (damage index), and Movies 8-10 (strain energy density), respectively.

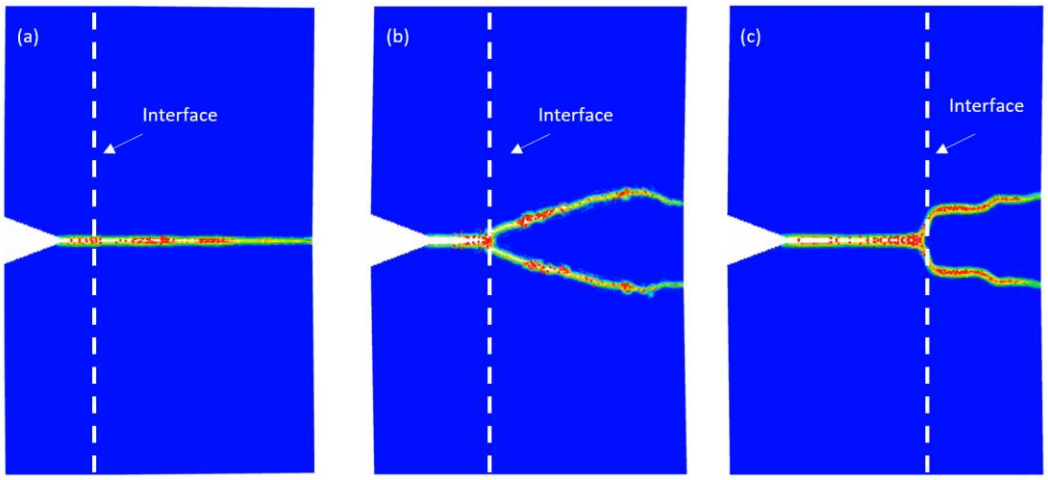

Figure 16 Damage map for bi-layered PMMA with the interface located at (a) 7 mm, (b) 17 mm, and (c) 42 mm from the tip of the pre-crack, respectively. See also Movies 5, 6, and 7 (damage index), and corresponding strain energy density in Movies 8, 9, and 10.

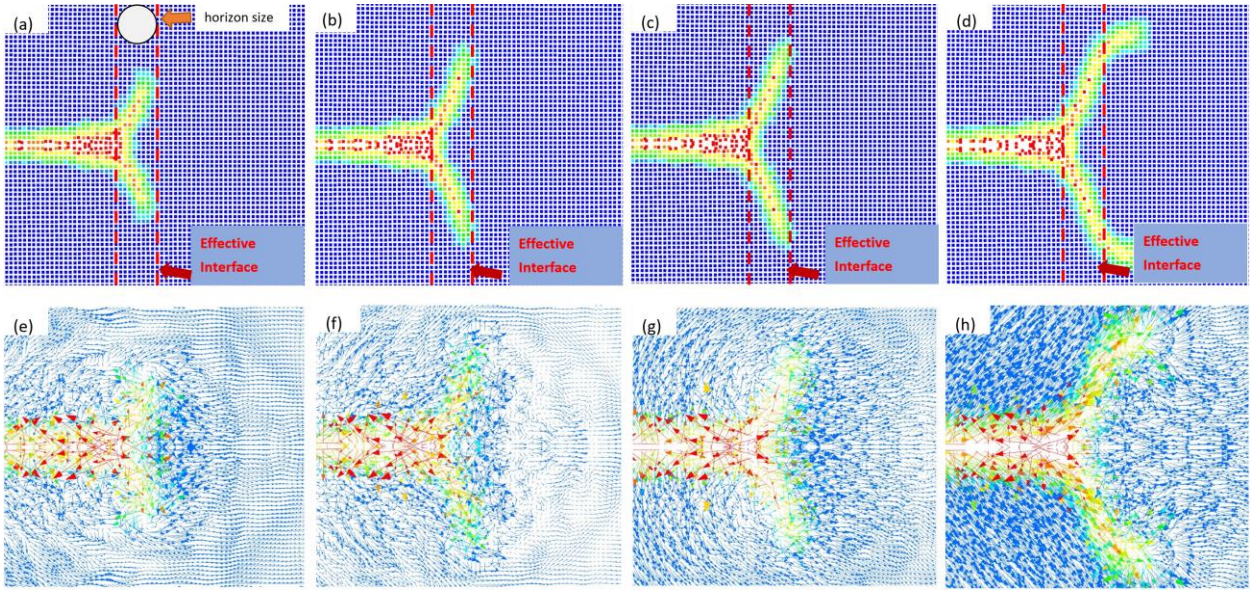

Figure 17 Zoomed-in view of nodal damage index maps (a)-(d) and nodal velocity vector plot (e)-(h) for bi-layered PMMA with the interface location at 42 mm at: 238 μs for (a) and (e), 250 μs for (b) and (f), and (c)(g) 262 μs, 286 μs for (d) and (h), from the moment loading is applied. The size of the horizon region is shown in (a). The limits of the interface effective thickness in the PD model are shown with red dashed lines in the top row. See also Movies 11 and 12.

Notice that in the computed results shown in Figure 16 and Figure 17**Error! Reference source not found.**, for the sample with interface location at 42 mm, the interface cracks are not perfectly vertical. This is because the interface is modeled by considering all bonds crossing the geometrical line of the actual interface as "interface bonds". This means that the effective thickness of the interface in our model is equal to twice the horizon size, and, for the horizon size used here, that is much larger than the actual thickness of the experimental sample (16 times thicker than the weak interface). This is why the computed interface cracks have a slight tilt. In the damage and nodal velocity vector plots around the interface location, shown in Figure 17, the lengths of the arrows are proportional to the nodal velocity magnitude values, and their color indicates the corresponding nodal damage index. The simulation movies corresponding to these plots are Movies 11 and 12.

In Figure 17, we show several snapshots of the crack growth near the interface. After branching, the cracks first grow along the interface and then change direction and penetrate into the second PMMA layer. In the results in [6] simulated using cohesive elements, the interface is damaged but penetration into the second PMMA layer does not happen. The nonlocal PD model captures an enlargement of the fracture process zone (see Figure 17) just before the main crack reaches the interface and branches, and once again when the crack traveling along the interface changes direction and penetrates into the second

PMMA layer. Experiments have shown that enlargement of the fracture process zone is a characteristic of crack branching in dynamic brittle fracture [54]. One can also observe some tilt through the experimental samples thickness for cracks penetrating into the second PMMA layer, visible as “whiter” crack portions in Figure 7 and Figure 8, at the entrance in the second layer, signatures of light being reflected from the rougher/twisted crack surfaces at those locations. A 3D model would likely show these twists, while here, in our 2D simulations, they are noticeable as wider damage along the crack paths. Models based on describing cracks as mathematical surfaces/curves can miss these aspects that are critical in correctly dissipating the right amount of energy as the dynamic cracks advance. This is where nonlocal models, as the PD one introduced here, show their relevance and benefits in dynamic brittle fracture.

In the damage maps shown in Figure 18**Error! Reference source not found.**, we notice that before the crack tip reaches the interface location, some damage initiates along the interface, at the mid-line through its thickness and develops into a crack. This is caused by stress waves interacting and creating mode I fracture conditions ahead of the crack tip. The velocity vector plots in Figure 18 show how nodes along the mid-line through the interface width have velocity vectors pointing in opposite directions, initially. This initial interface crack opens up in the material over a length similar to the width of the fracture process zone of the approach main crack is created. Once the main crack reaches the interface crack, it starts growing along the interface but in mixed mode, dominated by mode II conditions (see Figure 17). The dominant fracture mode switches again as the interface crack tips approach the second PMMA layer, as the dominant fracture mode is mode I again. Experimental observations (see [2] page 323) confirm that cracks are under mixed-mode fracture when propagating along the interface and switch to mode I after penetrating into the second layer.

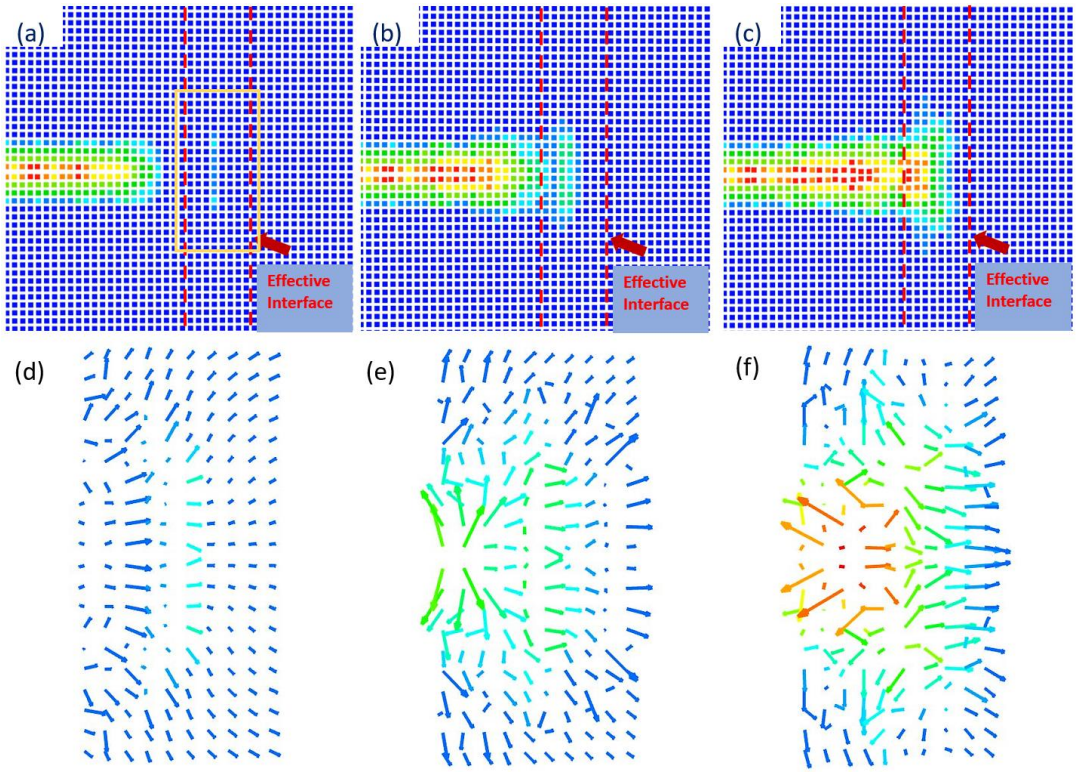

Figure 18 Zoomed-in view of damage map in (a)-(c), and velocity vector plot (color of arrows shows damage index values) in (d)-(f) for the yellow box area shown in (a) for the sample with the interface located at 42 mm. Snapshots in (a) and (d) taken at 218 μs, (b) and (e) at 222 μs, and (c) and (f) at 226 μs from the moment loading is applied. An interface crack develops before the main crack reaches there.

Comparison of histories of simulated crack propagation speeds with experimental measurements is shown in Figure 19. For all three cases, the computed crack velocity matches relatively well the profiles from experiments. For the case with the interface at 7 mm, the crack velocity is faster than the experimental results before 110 μs. For the case with interface at 17 mm, the crack velocity is slower at the beginning, but faster after crack branching. There are several potential reasons that the results do not match the experimental values closer: (a) the Poisson's ratio of the adhesive is not reported in the experimental paper; in the computations here we used the same value as that of PMMA; (b) differences between the boundary conditions used in the simulations and the experimental conditions, both along the notch and the top and bottom boundaries, e.g. free boundaries (outside of the loaded notch) used in

the PD model while putty strips used on the top and bottom edges in the experimental setup [2], which partially absorb waves reaching those boundaries.

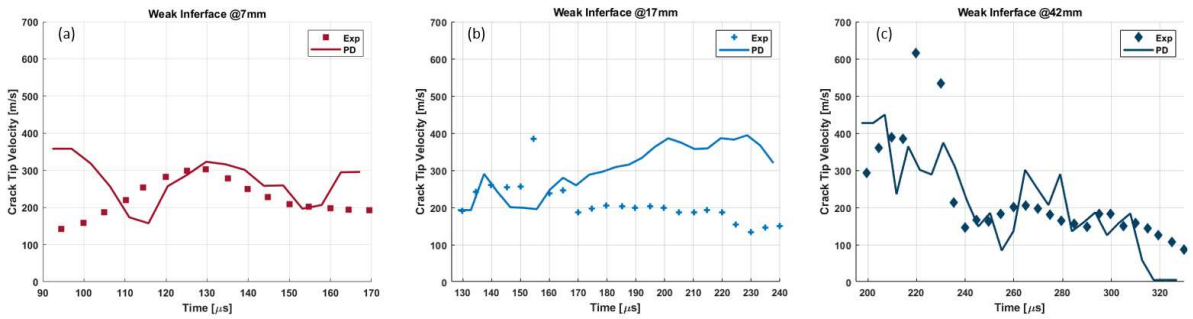

Figure 19 Comparisons of the histories of crack tip propagation speeds for bi-layered PMMA with the interface location at (a) 7 mm, (b) 17 mm, and (c) 42 mm show PD simulation match experimental measurements.

6. Conclusions

A peridynamic (PD) model for studying dynamic fracture in PMMA samples and the influence of location and fracture toughness of a material interface was introduced. Following some recent experimental results that point to the dramatic impact different interface fracture energies and different interface locations have on the dynamic fracture behavior of the PMMA system, we evaluate the performance of the PD model and its abilities to reproduce the complex behavior observed in experiments. Since the computational cost of explicitly modeling the very thin interface was high, we chose to model the interface at a larger scale. We treated all bonds crossing the interface line as “interface” bonds, leading to an effective interface width equal to twice the PD horizon size.

By testing various components in the model, we determined the three essential ones for correctly capturing dynamic brittle fracture in a PMMA system with interfaces: (1) softening around the crack tip to account for PMMA properties changing due to heat generated in rapidly running cracks; (2) independent fracture modes (mode I independent from mode II); (3) a bi-linear model for bond force-strain behavior that can match both fracture toughness and material strength for any PD horizon size (a bond-failure model with softening). We explained the influence of each of these components on the results. The heat-dependent stiffness of PMMA in dynamic fracture has a major influence on determining the crack propagation speed. The independent modes of fracture (mode I and II) are essential in capturing the correct mode-II dominated failure along the interface. The bi-linear (two-parameter) bond-failure

model allows for the correct crack initiation at the interface (a crack opens along the interface before the main crack reaches it) and into the second PMMA layer.

We varied the fracture toughness for the interface to match the values obtained experimentally with a thinner or thicker adhesive layer between the PMMA plates. The PD model results match, qualitatively, the influence of the interface toughness observed experimentally. The crack paths and angles of crack branching are also well captured. In particular, the computed results with the PD model show cracks travel significantly longer along the interface for the sample with a weaker interface, compared with the stronger one. The experimentally measured crack propagation velocities trends, including the velocities' increase when cracks move along the interface, are also well reproduced by the computational results from our model.

By changing the location of the weak interface in the PMMA bi-layer at a distance d = 7 mm, 17 mm, 42 mm from the pre-crack tip, our model captured the crack paths and crack tip velocities accurately and showed the trend, observed experimentally, that the propagating crack travels longer along the interface the farther away the interface is from the pre-crack tip location. The nonlocality in the PD model helps in showing that the fracture process zone is enlarged just before the crack reaches the interface, as it branches. After branching and running along the interface, the fracture process zone is again enlarged as the cracks penetrate into the second PMMA layer. A physical confirmation of this behavior is observable in the experimental results in the form of non-planar crack surfaces at their entrance in the second PMMA layer. It is unclear if local models of this problem would be able to capture such behavior, which is likely critical in predicting dynamic cracks' behavior in bi-layer PMMA structures. The new PD model introduced here helps us gain a better understanding of the mechanisms in dynamic fracture of PMMA with interfaces, and can provide insights when designing multi-layer PMMA structures.

Acknowledgments

This work has been supported by National Science Foundation under CDS&E CMMI award No. 1953346. This work was completed utilizing the Holland Computing Center of the University of Nebraska, which receives support from the Nebraska Research Initiative.

Appendix

To demonstrate the criticality of each of the model components discussed in Section 4, we show from PD models that lack as least one of the essential components. We also show results from a PD model in

which interface bonds are also softened, to mimic the potential sensitivity of the glue to rapidly propagating cracks.

Results from models missing at least one critical component

The PD model introduced in Section 4, three elements were called “critical”: (1) the HAZ that softens bonds around the crack tip to account for changes in PMMA mechanical properties due to heat generated by the rapidly propagating crack; (2) independent modes of fracture (mode I independent from mode II, achieved here by using a special case of a state-based model); and (3) a bi-linear model for bond-failure (bond-softening before final failure), capable to match both a given fracture toughness and the material strength, with any horizon size.

The influence of the HAZ has been studied in our previous study [20]. Without HAZ, the simulated crack propagation velocity in PMMA is around twice as fast as the experimentally measured values. In Figure 20, we compare the crack propagation velocity in the case with the interface at 7mm.

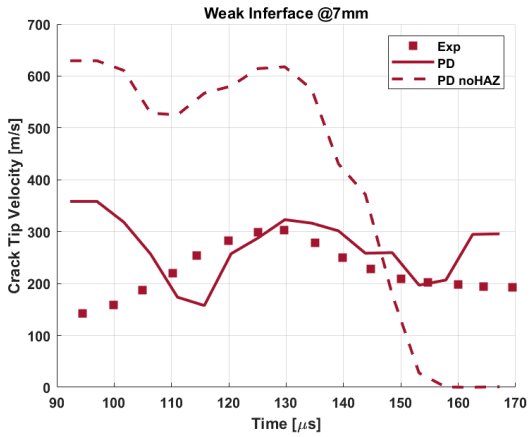

Figure 20 Comparisons of crack propagation speed (PD models with and without HAZ) in the bi-layered PMMA with the interface location at 7 mm. Experimental results from [2].

Having independent modes of fracture (mode I independent from mode II) is also critical to accurately capturing the mode-II dominated fracture along the interface. In Figure 21, we show the results from bond-based models in which the mode II fracture is not independent from mode I. We observe that for the cases with the interface located at 17 and 28 mm, the cracks do not branch at the interface, and do not run along the interface.

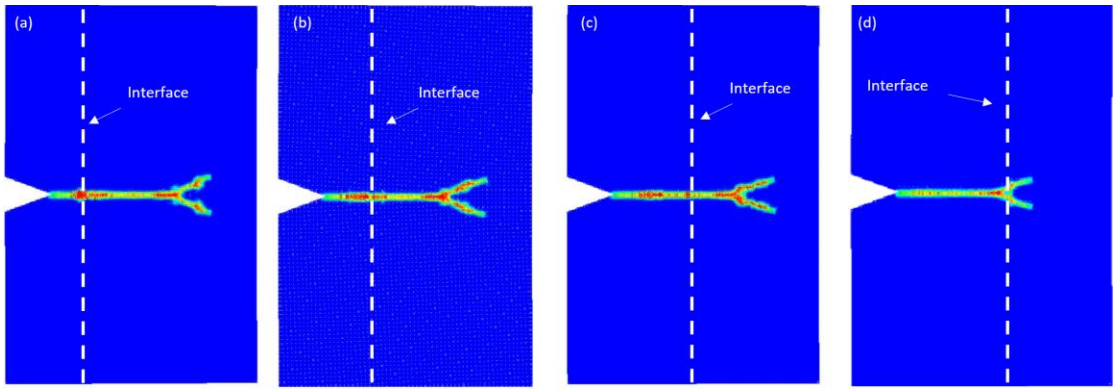

Figure 21 Damage maps at 240 μs (from the moment the loading is applied) obtained with the PD bond-based model (mode II not independent from mode I) for the bi-layered PMMA with interface location at: (a) 7 mm, (b) 17 mm, (c) 28 mm, and (d) 42 mm.

A bond-failure model that uses a sudden drop of bond force from its highest value to zero (a one-parameter bond-failure model) can only match, for a given horizon size, either the fracture toughness or the material strength. Using this model with a critical bond strain matched to the fracture toughness, for example, will match a material's strength for a particular size of the PD horizon. That size, however, may turn out to be extremely small and thus not usable for practical computations. A two-parameter bond-failure model, however, can match both the fracture toughness and the material strength, for any horizon size (see [50] for details). Matching material strength is critical in obtaining crack initiation at the correct stress levels in samples in which there are no pre-cracks. This is exactly our case in which we have crack initiation at the interface (before the main crack arrives there) and crack initiation into the second PMMA layer. Simulation results from a model that uses a one-parameter bond-damage model instead of the bi-linear model used in the main text of the paper are shown in Figure 22. While branching appears to happen at the interface for the 17, 28, and 42 mm, there is very little propagation along the interface.

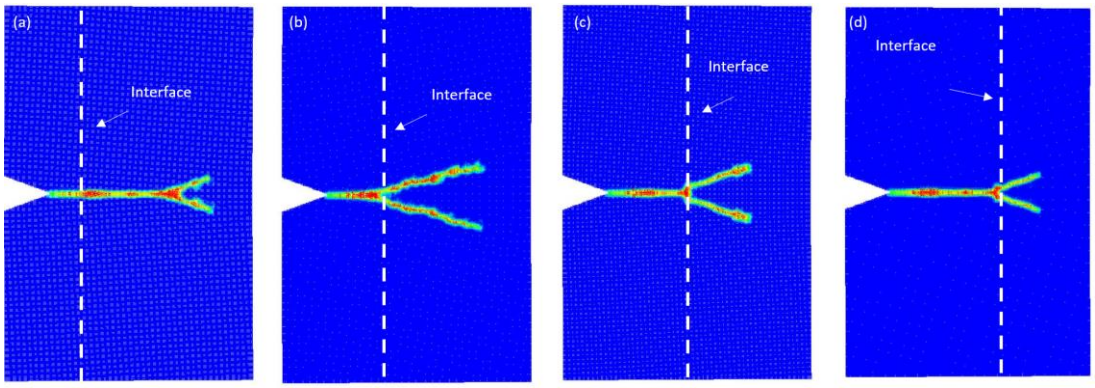

Figure 22 Damage maps at 240 μs (from the moment the loading is applied) from the PD model with a one-parameter bond-damage model for bi-layered PMMA with the interface location at: (a) 7 mm, (b) 17 mm, (c) 28 mm, and (d) 42 mm.

Results from model with heat-induced softening of interface bonds

While we do not have available data on the temperature variation of material properties for the glue material used in the PMMA bi-layered structure, it may be reasonable to assume a similar type of behavior as the HAZ model we used for PMMA. We therefore assume that interface bonds are affected by heat. In the model used here we do not include the independent modes of fracture (we use the bond-based model), nor the bi-linear bond-failure model. We hypothesize that the glue is more sensitive to the high temperatures caused by the rapid crack propagation, compared with PMMA. We use the bilinear model (pink dash line) shown in the figure below. The micromodulus of interface bonds decreases to $0.01c_{glue}$ when the bond strain is larger than $0.1s_0$.

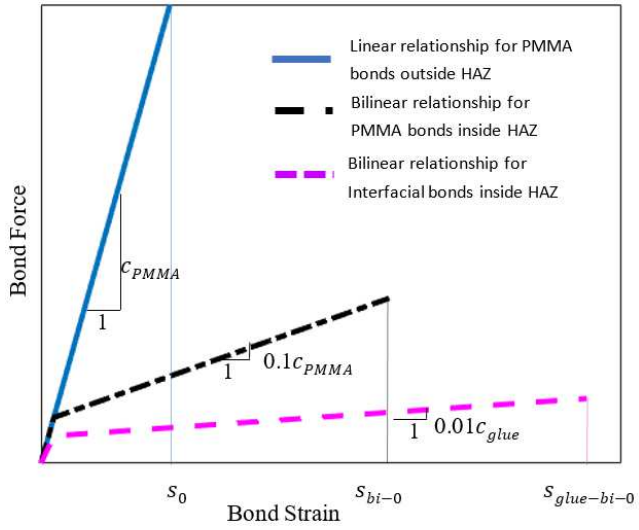

Figure 23 Heat-affected model for interface bonds.

The constitutive model for interface bonds in the HAZ is:

$$\boldsymbol{f}(\boldsymbol{\eta},\boldsymbol{\xi}) = \begin{cases} \dfrac{\boldsymbol{\eta}+\boldsymbol{\xi}}{\|\boldsymbol{\eta}+\boldsymbol{\xi}\|} c(\boldsymbol{\xi})[0.01s + 0.099s_0], & \text{if } s > 0.1s_0 \text{ and } \lambda_{HAZ} = 1 \\ \dfrac{\boldsymbol{\eta}+\boldsymbol{\xi}}{\|\boldsymbol{\eta}+\boldsymbol{\xi}\|} c(\boldsymbol{\xi})s, & \text{otherwise} \end{cases} \tag{39}$$

Similar to Eq. (37), to maintain the fracture energy G_0 the same, the following condition needs to be satisfied (areas under linear and bilinear functions need to match) for the interfacial bonds:

$$\frac{1}{2}{s_0}^2 = \frac{1}{2}(0.1s_0)^2 + (0.1s_0)\left(s_{glue-bi-0} - 0.1s_0\right) + \frac{1}{2}(0.01)\left(s_{glue-bi-0} - 0.1s_0\right)^2 \tag{40}$$

The critical strain $s_{glue-bi-0}$ for the bilinear function of interface bonds is $4.23s_0$.

With this model, the damage maps for PMMA samples with weak/strong interface and samples with different interface locations are shown below. The histories of the crack tip propagation speeds are

compared with experiments as well. In Figure 24 and Figure 25, the crack path and crack velocity of PMMA samples with weak/strong interface match well with the experiments.

However, since in the regular bond-based model (with one-parameter bond-failure model), the mode II fracture is not independent from mode I fracture, and the material strength will differ depending on the horizon size, mode II-dominated fracture and crack initiation along the interface are not going to be accurately captured. Indeed, as seen from Figure 26, the crack lengths along the interface obtained by these simulations, especially when d = 42 mm, are significantly smaller compared with the experimental results [2]. Also, when d = 7 mm, the crack branches inside the second layer of PMMA, which is not observed in experiments [2]. Since the HAZ in PMMA is considered here, crack propagation speeds, shown in Figure 25 and Figure 27 are in good agreement with experiments.

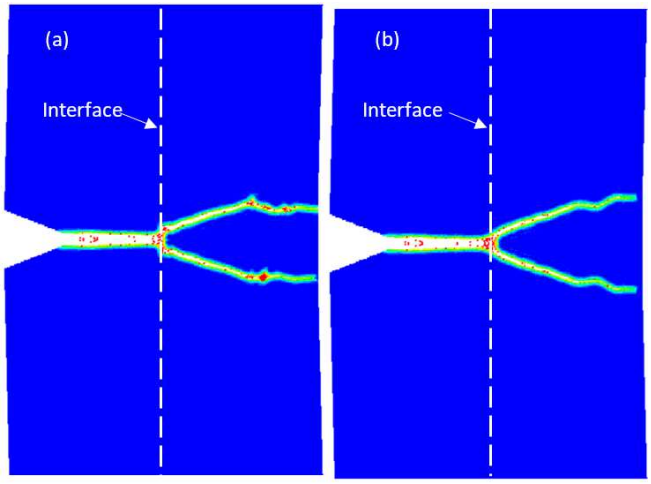

Figure 24 Damage maps from the bond-based PD model with heat-induced softening of interface bonds for bi-layered PMMA with: (a) weak interface, and (b) strong interface.

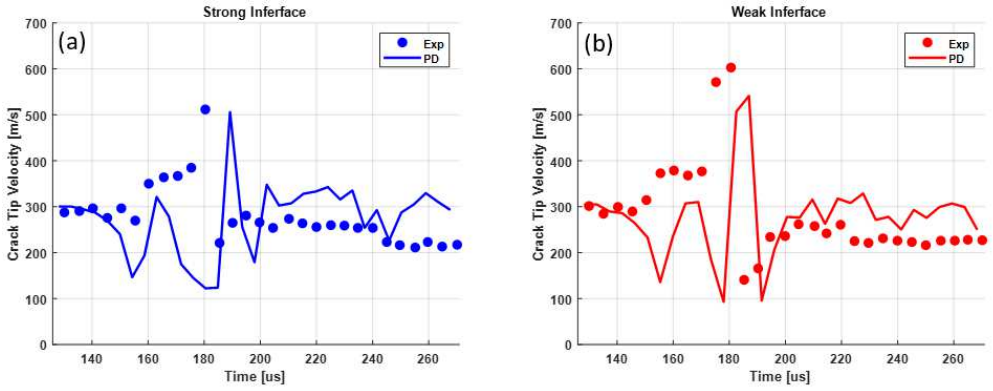

Figure 25 Comparisons between experimental results (from [3]*) and results obtained with the bond-based PD model with heat-induced softening of interface bonds for crack propagation speed in the bi-layered PMMA with: (a) strong interface, and (b) weak interface.*

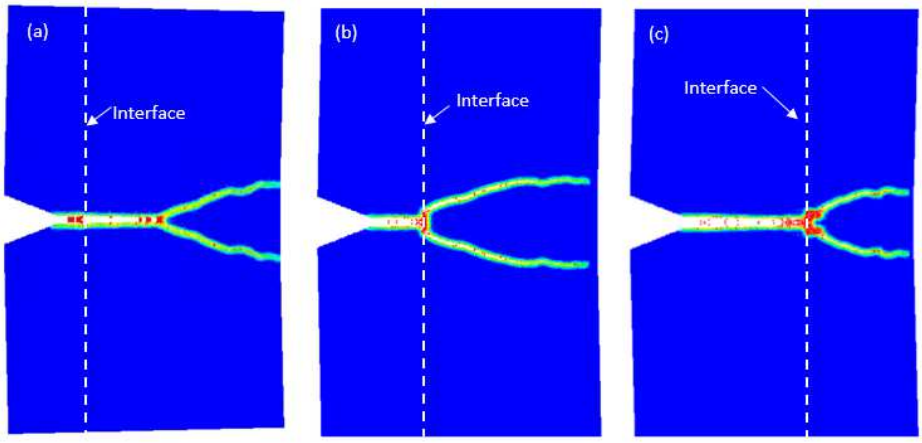

Figure 26 Damage maps from the bond-based PD model with heat-induced softening of interface bonds for bi-layered PMMA with the interface location at: (a) 7 mm, (b) 17 mm, and (c) 42 mm.

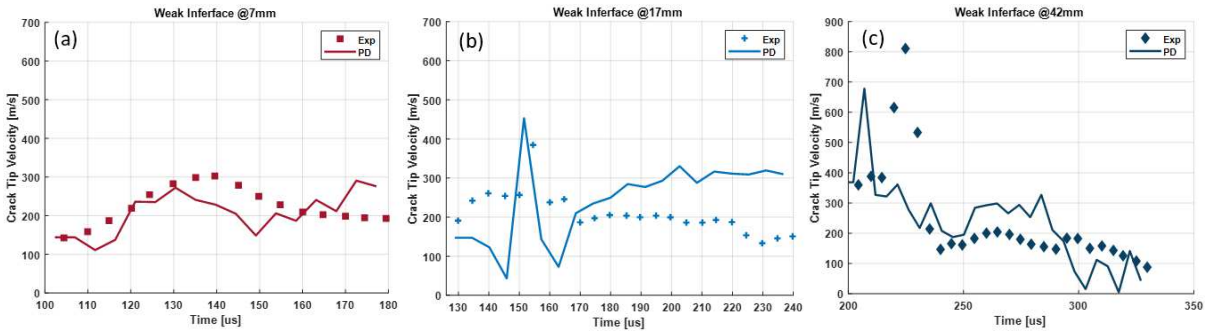

Figure 27 Comparisons between experimental results (from [2]*) and results obtained with the bond-based PD model with heat-induced softening of interface bonds crack propagation speed in the bi-layered PMMA with the interface location at: (a) 7 mm, (b) 17 mm, and (c) 42 mm.*

Reference

[1] S. Suresh, Y. Sugimura, and E. K. Tschegg, "The growth of a fatigue crack approaching a perpendicularly-oriented, bimaterial interface," *Scripta metallurgica et materialia*, vol. 27, no. 9, pp. 1189–1194, 1992, doi: 10.1016/0956-716X(92)90597-8.

[2] B. M. Sundaram and H. V Tippur, "Dynamics of crack penetration vs. branching at a weak interface: an experimental study," *J Mech Phys Solids*, vol. 96, pp. 312–332, 2016, doi: 10.1016/j.jmps.2016.07.020.

[3] B. M. Sundaram and H. V. Tippur, "Dynamic Crack Growth Normal to an Interface in Bi-Layered Materials: An Experimental Study Using Digital Gradient Sensing Technique," *Exp Mech*, vol. 56, no. 1, pp. 37–57, 2016, doi: 10.1007/s11340-015-0029-x.

[4] J. H. Song, H. Wang, and T. Belytschko, "A comparative study on finite element methods for dynamic fracture," *Comput Mech*, vol. 42, no. 2, pp. 239–250, 2008, doi: 10.1007/s00466-007-0210-x.

[5] X. Lu, B. Y. Chen, V. B. C. Tan, and T. E. Tay, "A separable cohesive element for modelling coupled failure in laminated composite materials," *Compos Part A Appl Sci Manuf*, vol. 107, pp. 387–398, 2018, doi: doi.org/10.1016/j.compositesa.2018.01.014.

[6] S. Dondeti and H. V Tippur, "A Hybrid Experimental-Numerical Study of Crack Initiation and Growth in Transparent Bilayers Across a Weak Interface," in *Dynamic Behavior of Materials, Volume 1*, 2019, pp. 57–63. doi: 10.1007/978-3-319-95089-1_7.

[7] F. Bobaru, Y. D. Ha, and W. Hu, "Damage progression from impact in layered glass modeled with peridynamics," *Central European Journal of Engineering*, vol. 2, no. 4, pp. 551–561, 2012, doi: 10.2478/s13531-012-0020-6.

[8] W. Hu, Y. Wang, J. Yu, C. F. Yen, and F. Bobaru, "Impact damage on a thin glass plate with a thin polycarbonate backing," *Int J Impact Eng*, vol. 62, pp. 152–165, 2013, doi: 10.1016/j.ijimpeng.2013.07.001.

[9] B. Ren, C. T. Wu, and E. Askari, "A 3D discontinuous Galerkin finite element method with the bond-based peridynamics model for dynamic brittle failure analysis," *Int J Impact Eng*, vol. 99, pp. 14–25, 2017, doi: 10.1016/j.ijimpeng.2016.09.003.

[10] M. Bußler *et al.*, "Visualization of fracture progression in peridynamics," *Computers and Graphics (Pergamon)*, vol. 67, pp. 45–57, 2017, doi: 10.1016/j.cag.2017.05.003.

[11] S. A. Silling, "Reformulation of elasticity theory for discontinuities and long-range forces," *J Mech Phys Solids*, vol. 48, no. 1, pp. 175–209, 2000, doi: 10.1016/S0022-5096(99)00029-0.

[12] S. Jafarzadeh, Z. Chen, and F. Bobaru, "Peridynamic modeling of intergranular corrosion damage," *J Electrochem Soc*, vol. 165, no. 7, p. C362, 2018, doi: 10.1149/2.0821807jes.

[13] S. Jafarzadeh, Z. Chen, and F. Bobaru, "Peridynamic modeling of repassivation in pitting corrosion of stainless steel," *Corrosion*, vol. 74, no. 4, pp. 393–414, 2018.

[14] J. Zhao, Z. Chen, J. Mehrmashhadi, and F. Bobaru, "A stochastic multiscale peridynamic model for corrosion-induced fracture in reinforced concrete," *Eng Fract Mech*, p. 106969, 2020, doi: 10.1016/j.engfracmech.2020.106969.

[15] J. Mehrmashhadi, Z. Chen, J. Zhao, and F. Bobaru, "A stochastically homogenized peridynamic model for intraply fracture in fiber-reinforced composites," *Compos Sci Technol*, vol. 182, p. 107770, 2019, doi: 10.1016/j.compscitech.2019.107770.

[16] S. Jafarzadeh, L. Wang., A. Larios, and F. Bobaru, "A fast convolution-based method for peridynamic transient diffusion in arbitrary domains," *Comput. Methods Appl. Mech. Engrg*, vol. 375, p. 113633, 2021, doi: 10.1016/j.cma.2020.113633.

[17] S. Jafarzadeh, L. Wang, A. Larios, and F. Bobaru, "A fast convolution-based method for peridynamic transient diffusion in arbitrary domains," *Comput Methods Appl Mech Eng*, vol. 375, p. 113633, 2021, doi: 10.1016/j.cma.2020.113633.

[18] L. Wang and F. Bobaru, "Connections Between the Meshfree Peridynamics Discretization and Graph Laplacian for Transient Diffusion Problems," *Journal of Peridynamics and Nonlocal Modeling*, vol. 3, no. 4, pp. 307–326, 2021, doi: 10.1007/s42102-021-00053-2.

[19] S. A. Silling and E. Askari, "A meshfree method based on the peridynamic model of solid mechanics," *Comput Struct*, vol. 83, no. 17–18, pp. 1526–1535, 2005, doi: 10.1016/j.compstruc.2004.11.026.

[20] J. Mehrmashhadi, L. Wang, and F. Bobaru, "Uncovering the dynamic fracture behavior of PMMA with peridynamics: The importance of softening at the crack tip," *Eng Fract Mech*, vol. 219, p. 106617, 2019, doi: 10.1016/j.engfracmech.2019.106617.

[21] G. Zhang, Q. Le, A. Loghin, A. Subramaniyan, and F. Bobaru, "Validation of a peridynamic model for fatigue cracking," *Eng Fract Mech*, vol. 162, pp. 76–94, 2016, doi: 10.1016/j.engfracmech.2016.05.008.

[22] S. A. Silling, M. Epton, O. Weckner, J. Xu, and E. Askari, "Peridynamic states and constitutive modeling," *J Elast*, vol. 88, no. 2, pp. 151–184, 2007, doi: 10.1007/s10659-007-9125-1.

[23] G. Sarego, Q. V Le, F. Bobaru, M. Zaccariotto, and U. Galvanetto, "Linearized state-based peridynamics for 2-D problems," *Int J Numer Methods Eng*, vol. 108, no. 10, pp. 1174–1197, 2016, doi: 10.1002/nme.5250.

[24] Y. L. Hu and E. Madenci, "Bond-based peridynamic modeling of composite laminates with arbitrary fiber orientation and stacking sequence," *Compos Struct*, vol. 153, pp. 139–175, 2016, doi: 10.1016/j.compstruct.2016.05.063.

[25] X. Zhou, Y. Wang, Y. Shou, and M. Kou, "A novel conjugated bond linear elastic model in bond-based peridynamics for fracture problems under dynamic loads," *Eng Fract Mech*, vol. 188, pp. 151–183, 2018, doi: 10.1016/j.engfracmech.2017.07.031.

[26] V. Diana and S. Casolo, "A bond-based micropolar peridynamic model with shear deformability: Elasticity, failure properties and initial yield domains," *Int J Solids Struct*, vol. 160, pp. 201–231, 2019, doi: 10.1016/j.ijsolstr.2018.10.026.

[27] Q. zhi Zhu and T. Ni, "Peridynamic formulations enriched with bond rotation effects," *Int J Eng Sci*, vol. 121, pp. 118–129, 2017, doi: 10.1016/j.ijengsci.2017.09.004.

[28] W. J. Li, Q. Z. Zhu, and T. Ni, “A local strain-based implementation strategy for the extended peridynamic model with bond rotation,” *Comput Methods Appl Mech Eng*, vol. 358, p. 112625, 2020, doi: 10.1016/j.cma.2019.112625.

[29] E. Madenci, A. Barut, and N. Phan, “Bond-Based Peridynamics with Stretch and Rotation Kinematics for Opening and Shearing Modes of Fracture,” *Journal of Peridynamics and Nonlocal Modeling*, pp. 1–44, 2021, doi: 10.1007/s42102-020-00049-4.

[30] Q. V Le and F. Bobaru, “Surface corrections for peridynamic models in elasticity and fracture,” *Comput Mech*, vol. 61, no. 4, pp. 499–518, 2018, doi: 10.1007/s00466-017-1469-1.

[31] E. Madenci, M. Dorduncu, A. Barut, and N. Phan, “A state-based peridynamic analysis in a finite element framework,” *Eng Fract Mech*, vol. 195, pp. 104–128, 2018, doi: 10.1016/j.engfracmech.2018.03.033.

[32] F. Bobaru, Y. D. Ha, and W. Hu, “Numerical integration in peridynamics,” Technical report, 2010.

[33] P. Seleson, “Improved one-point quadrature algorithms for two-dimensional peridynamic models based on analytical calculations,” *Comput Methods Appl Mech Eng*, vol. 282, pp. 184–217, 2014, doi: 10.1016/j.cma.2014.06.016.

[34] P. Wu, F. Yang, Z. Chen, and F. Bobaru, “Stochastically homogenized peridynamic model for dynamic fracture analysis of concrete,” *Eng Fract Mech*, vol. 253, no. April, p. 107863, 2021, doi: 10.1016/j.engfracmech.2021.107863.

[35] L. Verlet, “Computer" experiments" on classical fluids. I. Thermodynamical properties of Lennard-Jones molecules,” *Physical review*, vol. 159, no. 1, p. 98, 1967, doi: 10.1103/PhysRev.159.98.

[36] S. S. Rao, *Engineering optimization: theory and practice*. John Wiley & Sons, 2019.

[37] Z. Xu, G. Zhang, Z. Chen, and F. Bobaru, “Elastic vortices and thermally-driven cracks in brittle materials with peridynamics,” *Int J Fract*, vol. 209, no. 1–2, pp. 203–222, Jan. 2018, doi: 10.1007/s10704-017-0256-5.

[38] Y. Zhang and P. Qiao, “A new bond failure criterion for ordinary state-based peridynamic mode II fracture analysis,” *Int J Fract*, vol. 215, no. 1–2, pp. 105–128, 2019, doi: 10.1007/s10704-018-00341-x.

[39] K. N. G. Fuller, P. G. Fox, and J. E. Field, “The temperature rise at the tip of fast-moving cracks in glassy polymers,” *Proceedings of the Royal Society of London. A. Mathematical and Physical Sciences*, vol. 341, no. 1627, pp. 537–557, 1975, doi: 10.1098/rspa.1975.0007.

[40] E. J. Kramer and L. L. Berger, “Fundamental processes of craze growth and fracture,” in *Crazing in Polymers Vol. 2*, Springer, 1990, pp. 1–68. doi: 10.1007/BFb0018018.

[41] R. P. Wool, *Polymer Interfaces: Structure and Strength*. Hanser Pub Inc, 1995.

[42] S. Acharya and A. K. Mukhopadhyay, "High strain rate compressive behavior of PMMA," *Polymer Bulletin*, vol. 71, no. 1, pp. 133–149, 2014, doi: 10.1007/s00289-013-1050-9.

[43] A. A. Abdel-Wahab, S. Ataya, and V. V Silberschmidt, "Temperature-dependent mechanical behaviour of PMMA: Experimental analysis and modelling," *Polym Test*, vol. 58, pp. 86–95, 2017, doi: 10.1016/j.polymertesting.2016.12.016.

[44] I. H. Sahputra, A. Alexiadis, and M. J. Adams, "Temperature and configurational effects on the Young's modulus of poly (methyl methacrylate): a molecular dynamics study comparing the DREIDING, AMBER and OPLS force fields," *Mol Simul*, vol. 44, no. 9, pp. 774–780, 2018, doi: 10.1080/08927022.2018.1450983org/10.1080/08927022.2018.1450983.

[45] J. Crank, *The mathematics of diffusion*. Oxford university press, 1979.

[46] E. Kreyszig, *Advanced Engineering Mathematics*. Wiley, 2011.

[47] W.-C. Chen, S.-J. Lee, and B.-C. Ho, "Diffusion coefficients of acrylic monomers in poly (methyl methacrylate)," *Journal of Polymer Research*, vol. 5, no. 3, pp. 187–191, 1998, doi: 10.1007/s10965-006-0055-6.

[48] S. Basu and E. Van der Giessen, "A thermo-mechanical study of mode I, small-scale yielding crack-tip fields in glassy polymers," *Int J Plast*, vol. 18, no. 10, pp. 1395–1423, 2002, doi: 10.1016/S0749-6419(02)00009-8.

[49] A. G. Atkins, C. S. Lee, and R. M. Caddell, "Time-temperature dependent fracture toughness of PMMA - Part 1," *J Mater Sci*, vol. 10, no. 8, pp. 1381–1393, 1975, doi: 10.1007/BF00540829.

[50] S. Niazi, Z. Chen, and F. Bobaru, "Crack nucleation in brittle and quasi-brittle materials: A peridynamic analysis," *Theoretical and Applied Fracture Mechanics*, vol. 112, no. October 2020, p. 102855, 2021, doi: 10.1016/j.tafmec.2020.102855.

[51] F. Bobaru, M. Yang, L. F. Alves, S. A. Silling, E. Askari, and J. Xu, "Convergence, adaptive refinement, and scaling in 1D peridynamics," *Int J Numer Methods Eng*, vol. 77, no. 6, pp. 852–877, Feb. 2009, doi: 10.1002/nme.2439.

[52] Y. D. Ha and F. Bobaru, "Studies of dynamic crack propagation and crack branching with peridynamics," *Int J Fract*, vol. 162, no. 1–2, pp. 229–244, 2010, doi: 10.1007/s10704-010-9442-4.

[53] Y. D. Ha and F. Bobaru, "Characteristics of dynamic brittle fracture captured with peridynamics," *Eng Fract Mech*, vol. 78, no. 6, pp. 1156–1168, 2011, doi: 10.1016/j.engfracmech.2010.11.020.

[54] K. Ravi-Chandar and B. Yang, "On the role of microcracks in the dynamic fracture of brittle materials," *J Mech Phys Solids*, vol. 45, no. 4, pp. 535–563, 1997.

Supplementary Files

This is a list of supplementary files associated with this preprint. Click to download.

- Movie1.mp4
- Movie2.mp4
- Movie3.mp4
- Movie4.mp4
- Movie5.mp4
- Movie6.mp4
- Movie7.mp4
- Movie8.mp4
- Movie9.mp4
- Movie10.mp4
- Movie11.mp4
- Movie12.mp4